J. Fluid Mech. (2004), *vol.* 518, *pp.* 281–317.
DOI: 10.1017/S0022112004001144 Printed in the United Kingdom

Numerical simulation of turbulent drag reduction using rigid fibres

By J. S. PASCHKEWITZ[1], YVES DUBIEF[2], COSTAS D. DIMITROPOULOS,[1,2] ERIC S. G. SHAQFEH[1,3] AND PARVIZ MOIN[2,3]

[1]Department of Chemical Engineering, Stanford University, CA 94305, USA

[2]Center for Turbulence Research, Stanford University, CA 94305, USA

[3]Department of Mechanical Engineering, Stanford University, CA 94305, USA

(Received 18 July 2003 and in revised form 2 July 2004)

We present a study of the drag reduction induced by rigid fibres in a turbulent channel flow using direct numerical simulation. The extra stresses due to the fibres are calculated with the well-known constitutive equation involving the moments of the orientation vector. Drag reductions of up to 26% are calculated, with the largest drag reductions observed using non-Brownian fibres and semi-dilute concentrations. These findings suggest that elasticity is not necessary to achieve turbulent drag reduction. Flow statistics show trends similar to those observed in simulation of polymeric drag reduction: Reynolds stresses are reduced, velocity fluctuations in the wall-normal and spanwise directions are reduced while streamwise fluctuations are increased, and streamwise vorticity is reduced. We observe strong correlations between the fibre stresses and inter-vortex extensional flow regions. Based on these correlations and instantaneous visualizations of the flow field, we propose a mechanism for turbulent drag reduction by rigid fibre additives.

1. Introduction

The reduction of turbulent drag has been observed experimentally in suspensions involving a wide array of materials; these include paper and cloth pulp (Robertson & Mason 1957; Radin, Zakin & Patterson 1975), asbestos (McComb & Chan 1985), colloidal crystals (Pirih & Swanson 1972; Radin *et al.* 1975), and chopped nylon (Lee, Vaseleski & Metzner 1974). Some of these materials, such as short nylon fibres and colloidal crystals, can be considered to be rigid rods to an excellent approximation. Additionally, Sasaki (1991) observed drag reduction using dilute solutions of xanthan gum and schizophyllum polysaccharide molecules having lengths comparable to their persistence lengths. Under these conditions, these polymers can also be modelled as rigid rods. These additives have not been as extensively investigated as flexible polymers since they typically yield low drag reductions or require larger concentrations to achieve the same drag reductions as those obtained with flexible polymer additives.

However, fibrous additives are more resistant to shear degradation than flexible polymers. This robustness has led investigators to consider mixtures of fibres and polymers in an attempt to develop an additive blend that is more shear-resistant than flexible polymers alone. These mixtures not only exhibit greater shear resistance, but also dramatically improved drag reduction properties. Lee *et al.* (1974) were the first to observe a synergistic effect where drag reductions using mixtures of polymer

and fibres exceeded the sum of the drag reductions using either additive alone. This synergistic effect was observed using both flexible asbestos and rigid nylon fibres. They also were able to exceed the maximum drag reduction asymptote of Virk, Mickley & Smith (1970). This effect was also observed by other investigators using both polymer–fibre mixtures (Malhotra, Deshmukh & Singh 1987) and mixtures of rigid and flexible polymers (Dingilian & Ruckenstein 1974; Reddy & Singh 1985). This synergy led Metzner (Kale & Metzner 1976; Metzner 1977) to speculate that fibres and polymers reduced turbulent drag by different mechanisms and that the action of fibres was related to extensional resistance in near-wall turbulent structures, which were poorly characterized at that time.

Our knowledge of near-wall turbulence and its relation to drag has been considerably enhanced in the last decade via direct numerical simulation. Kravchenko, Choi & Moin (1993) quantitatively demonstrated that skin friction was associated with near-wall vortex structures, with regions of high skin friction on the wall associated with downwash of high-speed fluid. Jimenez & Pinelli (1999) demonstrated that downwash of high-speed fluid due to these near-wall vortex structures is also associated with the formation of alternating high- and low-speed streaky structures between the wall and $y^+ \simeq 10$. Jimenez & Pinelli (1999) also showed that near-wall turbulence is self-sustaining: the streaks are unstable and act to generate vortices, which in turn advect high-speed fluid towards the wall generating the streaks. Turbulent drag can be reduced by disrupting either part of this cycle, as demonstrated in the numerical studies of vortex disruption using localized suction and blowing by Choi, Moin & Kim (1994) and streak disruption via application of a transverse body force by Lee & Kim (2002).

Numerical simulation has provided new understanding of the origins of drag reduction by polymer additives. Using constitutive models for the polymer stress, Sureshkumar, Beris & Handler (1997) and Dimitropoulos, Sureshkumar & Beris (1998) were able to obtain numerical simulations of polymer-induced drag reduction that were in qualitative agreement with experiments. Recent numerical simulations at Stanford (Terrapon *et al.* 2004; Dubief 2002; Dubief *et al.* 2003, 2004) have shown correlations between polymer stretch and near-wall coherent structures. However, with the exception of the preliminary work of den Toonder *et al.* (1997), there are no similar investigations of the mechanisms for drag reduction using constitutive relations for rigid fibrous or rodlike polymeric additives.

There have been several simulations of fibre flows in turbulent channel flow (Fan & Ahmadi 2000; Zhang *et al.* 2001), but these simulations are typically focused on aerosol deposition in gas flows and do not include the coupling of the fibre stresses to the fluid momentum calculation. There have also been numerical and experimental investigations of the interaction of spherical particles with turbulent gas and liquid flows (e.g. Li *et al.* 2001; Ahmed & Elgobashi 2000; Kulick, Fessler & Eaton 1994). These studies demonstrate that the presence of particles can substantially modify the flow field, with a strong size effect: small particles ($\approx 1 \times 10^{-7}$ m) reduce turbulence intensity while large particles ($\approx 1 \times 10^{-3}$ m) increase turbulence. Non-spherical particles would be expected to generate strongly anisotropic stresses not observed using spheres and for sufficiently small particles, the elastic stresses due to Brownian rotations could also be significant.

There have been several attempts to investigate the importance of these elastic stresses on fibre-induced drag reduction using simplified simulations. Den Toonder *et al.* (1997) investigated the relative importance of anisotropic stress and elasticity on drag reduction in polymeric solutions. To investigate the former, they performed

direct numerical simulations of a turbulent pipe flow using the non-Brownian rigid rod constitutive equation, but because of computational limitations, they used the simplifying assumption that the local fibre orientation was the local velocity vector. This fully aligned fibre assumption is questionable for a rapidly time-varying turbulent flow. Azaiez (2000) has demonstrated that stabilization of a free shear flow using fibrous additives is actually related to deviations from full alignment. Despite the local alignment assumption, den Toonder *et al.* (1997) were able to simulate modest drag reductions and obtain flow statistics that qualitatively agreed with experimental data for polymeric drag reduction. Using an *ad hoc* elasticity model, they also demonstrated that elasticity apparently decreased drag reduction, but the authors did not provide an explanation for this effect. Manhart (2003) performed uncoupled Lagrangian simulations of Brownian spheroids in a turbulent channel flow and found that increasing the elasticity increased the average stress values, but decreased the fluctuations of the extra stress, which were conjectured to be related to drag reduction. The lack of coupling to the flow calculation in the study by Manhart (2003) limits the insight obtainable from these results as the modification of the turbulent flow structures by the particles would be expected to have a significant impact on the particle dynamics and thus the mechanisms of drag reduction.

For the case of flexible polymer additives, Beris and coworkers (Sureshkumar *et al.* 1997; Dimitropoulos *et al.* 1998, 2001; Beris & Dimitropoulos 1999) obtained considerable insight into both the origins of the drag reduction effect and the role of additive elasticity. They showed a strong correlation between the extensional viscosity enhancement due to the additives and the weakening of the near-wall turbulence structures using a variety of statistical measures. Their work supports the elongational resistance hypothesis of Lumley (1969) and Seyer & Metzner (1969), both of whom speculated that drag reduction occurs when polymers undergo a coil–stretch transition, giving rise to large resistances to extensional flows associated with near-wall vortex structures. They found that the critical Weissenberg number, or the ratio of the polymer relaxation to characteristic flow time scales, must be of order 10 for drag reduction to occur. This result would suggest that the additive must possess some finite amount of elasticity (i.e. a non-zero relaxation time) in order for drag reduction to occur. An alternative argument for the necessity of additive elasticity was made by Tabor & deGennes (1986), who claimed that drag reduction is associated with the storage of elastic energy in the polymer molecules and the resulting disruption of the energy cascade. Joseph (1990) and Sreenivasan & White (2000) present theoretical arguments in favour of the elastic theory of Tabor & deGennes (1986). The experimental work of Sasaki (1991) using xanthan gum showed that increasing polymer flexibility, and thus increasing the elasticity, increases drag reduction effectiveness.

However, experimental studies (Lee *et al.* 1974; Radin *et al.* 1975) have shown that macroscopic, non-Brownian fibres (that have no elasticity) are capable of reducing drag in turbulent flows. These results would suggest that additive elasticity is not a requirement for drag reduction behaviour at all. Direct numerical simulations of Brownian rigid fibres and their action in turbulent flow allow the investigation of the role of elasticity through variation of the orientational diffusivity or in dimensionless terms, the rotary Péclet number, in a physically meaningful manner that is not possible using flexible polymer models. Determining the importance of additive elasticity on drag-reduction performance is one of the primary motivations of the present work.

In this paper, we present a systematic numerical investigation of drag reduction in a turbulent channel flow using rigid fibrous additives. We have studied suspensions

of rigid particles from dilute to semi-dilute concentrations and over a range of rotary Péclet number. In § 2, we discuss the constitutive equations for Brownian rigid fibres and the approximations we use in solving them. Details of the numerical methods used, including a study of box size and grid resolution, are presented in § 3. In § 4, turbulence statistics and structure for a representative drag-reduced flow are presented. A mechanism for drag reduction using rigid fibrous additives is presented in § 5. An examination of the effects of the closure approximation and the variation of the rheological parameters on drag-reduction effectiveness is presented in § 6 and followed by a summary in § 7.

2. Problem formulation

2.1. *Governing equations*

The flow is described with Cauchy's equations of motion for an incompressible fluid, and using indicial notation we have:

$$\frac{\partial u_i}{\partial x_i} = 0, \tag{2.1}$$

$$\rho\left(\frac{\partial u_i}{\partial t} + u_j\frac{\partial u_i}{\partial x_j}\right) = -\frac{\partial P}{\partial x_i} + \frac{\partial \tau_{ij}}{\partial x_j}, \tag{2.2}$$

where ρ is the fluid density and P is the pressure. The stress tensor is decomposed into the Newtonian and fibre contributions such that:

$$\tau = \tau^N + \tau^F = \mu\left(\frac{\partial u_i}{\partial x_j} + \frac{\partial u_j}{\partial x_i}\right) + \tau^F. \tag{2.3}$$

To describe the fibre contribution to the extra stress, we relate the stress to a description of the suspension microstructure.

2.2. *Constitutive equations*

We consider fibres that are rigid neutrally buoyant bodies of revolution with a length l, half-length L and characteristic (maximum) diameter D suspended in a Newtonian incompressible liquid. The orientation of the fibres is denoted using a unit vector p_i and the aspect ratio of the particle is defined as $r_e = l/D$. The orientational diffusivity due to Brownian rotation is denoted by d. The concentration of the fibres is defined using the volume fraction ϕ or the concentration parameter nL^3, where n is the number density of particles. We begin by assuming that the suspension is dilute, or that $nL^3 < 1$, but will also consider the semidilute case of $1 < nL^3 \ll r_e$ in the development of our model.

We assume that all inertial effects on the scale of the particle are negligible. One estimate of the particle Reynolds or Stokes number can be made using the magnitude of the velocity fluctuations; using a value of $0.1U_c$ and a particle length of ≈ 1 cm, we estimate the particle Reynolds number to be ≈ 2000 for the nylon fibres used by Lee *et al.* (1974). For this large particle Reynolds number, the negligible inertia assumption is clearly invalid and we expect that our model will not accurately capture the behaviour of such a system. Investigations into particle inertia show that the rotational dynamics of the particle can be substantially affected. Feng & Joseph (1995) showed that adding unsteady inertia terms to the fibre orientation evaluation and fluid flow equations tended to suppress Jeffrey orbits in Poiseuille flow. Using lattice-Boltzmann simulations, Qi & Luo (2002) showed that as the

particle Reynolds number is increased, the dynamics change from Jeffrey orbits to log-rolling with the long axis parallel to the vorticity vector. Additionally, as discussed in the review of inertial suspensions by Koch & Hill (2001), finite particle inertia causes particles to both experience an additional lift force and accumulate in low-vorticity regions. In these regions they clump densely, such that lubrication forces between particles should also be considered. None of these effects is considered in our analysis.

We also assume that the fibre length is much smaller than all scales of the turbulent flow. This assumption is poor for comparison to experiments with macroscopic fibres: for the turbulent pipe flow of Lee *et al.* (1974), we estimate the viscous length to be approximately 1×10^{-4} m, while the nylon fibres of interest had an average length of ≈ 1 cm. In order to account for non-homogeneous flow fields on the scale of the fibre, it will be necessary to use a non-local formulation of the fibre rheology as derived by Schiek & Shaqfeh (1995). This formulation requires explicit solution of the fibre orientation distribution function and was not used in our study.

For rigid biomolecules such as those used by Sasaki (1991), the viscous length is 2 to 3 orders of magnitude greater than the length of the molecule. Using a contour length of 1×10^{-6} m and the characteristic velocity reported in Lee *et al.* (1974), we obtain a particle Reynolds number of 0.2. For these additives, particle inertia and non-local effects are negligible. The analysis we present here is therefore strictly only valid for very small rodlike objects such as rigid biopolymers or microscopic colloidal particles.

With the aforementioned assumptions, the evolution of the orientation of a single fibre ($\dot{p}_i$) is described by Jeffrey's equation, and the Fokker–Planck equation describes the conservation of probability of orientation, $\Psi(\boldsymbol{p}, \boldsymbol{x}, t)$, where we have neglected centre of mass diffusion and assumed spatial homogeneity of the centres of mass:

$$\dot{p}_i = \Omega_{ij} p_j + \beta(E_{ij} p_j - p_i p_j E_{jk} p_k), \tag{2.4}$$

$$\frac{\mathrm{D}\Psi}{\mathrm{D}t} + \frac{\partial(\dot{p}_i \Psi)}{\partial p_i} = \mathrm{d}\frac{\partial^2 \Psi}{\partial p_k \partial p_k}, \tag{2.5}$$

where:

$$\Omega_{ij} = \frac{1}{2}\left(\frac{\partial u_j}{\partial x_i} - \frac{\partial u_i}{\partial x_j}\right), \tag{2.6}$$

$$E_{ij} = \frac{1}{2}\left(\frac{\partial u_j}{\partial x_i} + \frac{\partial u_i}{\partial x_j}\right). \tag{2.7}$$

In (2.5), $\partial/\partial p_i$ denotes the gradient in orientation space (Advani & Tucker 1987).

It is possible to solve the Fokker–Planck equation for the orientation distribution function directly and then calculate the necessary moments of fibre orientation to obtain the extra stress in either a completely Eulerian or coupled Eulerian–Lagrangian framework (e.g. Nayak 1998; Suen, Joo & Armstrong 2002). Because of the computational expense in either direct integration of the Fokker–Planck equation for the fibre orientation or the implementation of the 'double Lagrangian' method (Szeri & Leal 1994) in combination with the large number of particle trajectories required to obtain values of stress at any point in the flow field, we have chosen not to use this method. Instead, we use the orientation tensor formulation and solve for the second moment of p_i. This method is analogous to the solution for the

conformation tensor with the FENE or FENE-P models used in simulations of drag reductions with polymers (Sureshkumar *et al.* 1997).

The second and fourth moments of the orientation vector p_i are defined as (Hinch & Leal 1976):

$$\int p_i p_j \Psi \, \mathrm{d}\boldsymbol{p} = \langle pp \rangle = a_{ij}, \tag{2.8}$$

$$\int p_i p_j p_k p_l \Psi \, \mathrm{d}\boldsymbol{p} = \langle pppp \rangle = a_{ijkl}. \tag{2.9}$$

The evolution equation for the second moment as derived from (2.5) is given by Hinch & Leal (1976), in which E_{ij} is twice the value in (2.7):

$$\frac{\mathrm{D}a_{ij}}{\mathrm{D}t} = a_{ik}\frac{\partial u_j}{\partial x_k} + a_{kj}\frac{\partial u_i}{\partial x_k} + \frac{\beta - 1}{2}(E_{ik}a_{kj} + a_{ik}E_{kj}) - \beta E_{kl}a_{ijkl} + 2d(\delta_{ij} - 3a_{ij}). \tag{2.10}$$

The parameter β is defined as:

$$\beta = \frac{(r_e^2 - 1)}{(r_e^2 + 1)}. \tag{2.11}$$

Equation (2.10) contains the fourth moment a_{ijkl}. The evolution equation for any moment will contain terms proportional to the next higher moments (Advani & Tucker 1987). In order to close the set of equations at this order of approximation, a closure approximation relating a_{ijkl} to a_{ij} is required.

We have considered two closures in this work. The first is the three-dimensional hybrid closure of Advani & Tucker (1990), which is a weighted average of the linear (equation (2.14)) and quadratic (first term in equation (2.12)) closures. This closure has been shown to be more accurate than either the linear or quadratic closures in simple flows, while maintaining the stable and physical dynamic behaviour of the latter. The hybrid closure has the general form:

$$a_{ijkl} = f a_{ij}a_{kl} + (1 - f)b_{ijkl}. \tag{2.12}$$

For the three-dimensional problem, the forms of f and b_{ijkl} are:

$$f = 1 - 27\det(a_{ij}), \tag{2.13}$$

$$b_{ijkl} = -\tfrac{1}{35}(\delta_{ij}\delta_{kl} + \delta_{ik}\delta_{jl} + \delta_{il}\delta_{jk}) + \tfrac{1}{7}(a_{ij}\delta_{kl} + a_{ik}\delta_{jl} + a_{il}\delta_{jk} + a_{kl}\delta_{ij} + a_{jl}\delta_{ik} + a_{jk}\delta_{il}). \tag{2.14}$$

However, compared to more sophisticated closures, the hybrid closure has been shown to overpredict both the rate and degree of fibre alignment in simple flows (Chung & Kwon 2001), which would be expected to affect the stresses and resulting flow dynamics. For this reason, we have also considered the invariant-based optimal fitting (IBOF) closure of Chung & Kwon (2002), which is arguably the best closure available at present. This closure exhibits the nearly exact correspondence to explicit solutions of the Fokker–Planck equation predicted using eigenvalue-based fitting schemes such as the orthotropic weighted closure of Cintra & Tucker (1995) in simple shear, extension, and mixed flows, but does not exhibit the oscillatory behaviour of these methods at high rotary Péclet number. Chung & Kwon (2002) have also shown the IBOF closure has significantly less computational cost than the eigenvalue-based methods.

The IBOF closure expresses the symmetric fourth-order tensor a_{ijkl} as an expansion in the second-order tensor a_{ij} and the identity tensor δ_{ij} as derived using the Cayley–Hamilton theorem:

$$\begin{aligned} a_{ijkl} = {} & \beta_1 \mathrm{S}(\delta_{ij}\delta_{kl}) + \beta_2 \mathrm{S}(\delta_{ij}a_{kl}) + \beta_3 \mathrm{S}(a_{ij}a_{kl}) + \beta_4 \mathrm{S}(\delta_{ij}a_{km}a_{ml}) \\ & + \beta_5 \mathrm{S}(a_{ij}a_{km}a_{ml}) + \beta_6 \mathrm{S}(a_{im}a_{mj}a_{kn}a_{nl}), \end{aligned} \tag{2.15}$$

where the operator S denotes the symmetric part of the argument:

$$\begin{aligned} \mathrm{S}(T_{ijkl}) = {} & \tfrac{1}{24}[T_{ijkl} + T_{jikl} + T_{ijlk} + T_{jilk} + T_{klij} + T_{lkij} + T_{klji} + T_{lkji} + T_{ikjl} + T_{kijl} \\ & + T_{jlik} + T_{ljik} + T_{jlki} + T_{ljki} + T_{iljk} + T_{lijk} + T_{ilkj} + T_{likj} + T_{jkil} + T_{kjil} \\ & + T_{jkli} + T_{kjli} + T_{iklj} + T_{kilj}]. \end{aligned} \tag{2.16}$$

The IBOF closure assumes that the coefficients β_1 to β_6 are functions of the second and third invariants of the tensor a_{ij}. These invariants are the square and determinant of a_{ij}, and are denoted as II and III, respectively. Chung & Kwon (2002) derived analytical expressions for three of the β_i values and used fifth-order polynomial fittings in terms of the invariants for the remaining three:

$$\begin{aligned} \beta_1 = {} & \tfrac{3}{5}\big[-\tfrac{1}{7} + \tfrac{1}{5}\beta_3\left(\tfrac{1}{7} + \tfrac{4}{7}II + \tfrac{8}{3}III\right) - \beta_4\left(\tfrac{1}{5} - \tfrac{8}{15}II - \tfrac{14}{15}III\right) \\ & - \beta_6\left(\tfrac{1}{35} - \tfrac{24}{105}III - \tfrac{4}{35}II + \tfrac{16}{15}II(III) + \tfrac{8}{35}II^2\right)\big], \end{aligned} \tag{2.17}$$

$$\beta_2 = \tfrac{6}{7}\big[1 - \tfrac{1}{5}\beta_3(1 + 4II) + \tfrac{7}{5}\beta_4\left(\tfrac{1}{6} - II\right) - \beta_6\left(-\tfrac{1}{5} + \tfrac{2}{3}III + \tfrac{4}{5}II - \tfrac{8}{5}II^2\right)\big], \tag{2.18}$$

$$\beta_5 = -\tfrac{4}{5}\beta_3 - \tfrac{7}{5}\beta_4 - \tfrac{6}{5}\beta_6\left(1 - \tfrac{4}{3}II\right); \tag{2.19}$$

while $\beta_{3,4,6}$ are obtained using:

$$\begin{aligned} \beta_i = {} & a(i,1) + a(i,2)II + a(i,3)II^2 + a(i,4)III + a(i,5)III^2 + a(i,6)(II)(III) \\ & + a(i,7)II^2III + a(i,8)(II)(III)^2 + a(i,9)II^3 + a(i,10)III^3 + a(i,11)II^3III \\ & + a(i,12)II^2III^2 + a(i,13)(II)III^3 + a(i,14)II^4 + a(i,15)III^4 + a(i,16)II^4III \\ & + a(i,17)II^3III^2 + a(i,18)II^2III^3 + a(i,19)(II)III^4 + a(i,20)II^5 \\ & + a(i,21)III^5 \quad (i = 3, 4, 6). \end{aligned} \tag{2.20}$$

The 21 fitting coefficients for each of these three β_i values were obtained by using a least-squares fitting to the exact solutions of the Fokker–Planck equation in a variety of simple flows. The values of the fitting coefficients are provided in an appendix to Chung & Kwon (2002). We compare the results obtained using this more accurate but computationally expensive closure with those obtained with the hybrid closure in § 6. We have observed that the IBOF closure is significantly more computationally expensive than the hybrid closure, and as a result, we have chosen to use the hybrid closure to determine the appropriate simulation parameters and to investigate the effect of varying the suspension rheological properties. We have used the more accurate IBOF closure to calculate the drag-reduced flow statistics presented in § 4 and mechanisms of drag reduction in § 5.

2.3. *Stress tensor*

The divergence of the extra stress due to the fibres is used to couple the effect of the fibres into the flow simulation. We consider the viscous and elastic contributions to the stress tensor separately. To calculate the exact extra stress, we now must limit ourselves to a specific particle shape and we choose prolate spheroids.

Hinch & Leal (1975, 1976) obtained the viscous stress tensor for spheroids:

$$\tau_{ij}^{visc} = 2\mu\phi(2AE_{lk}a_{ijkl} + 2B(E_{ik}a_{kj} + a_{ik}E_{kj}) + CE_{ij}), \tag{2.21}$$

where ϕ is the volume fraction, μ is the solvent viscosity, and A, B and C are functions of the aspect ratio and are given for the limit $r_e \to \infty$ in Hinch & Leal (1972). These functions are:

$$A = \frac{r_e^2}{4\left(\ln(2r_e) - \frac{3}{2}\right)}, \tag{2.22}$$

$$B = \frac{3\ln(2r_e) - \frac{11}{2}}{r_e^2}, \tag{2.23}$$

$$C = 2. \tag{2.24}$$

In the case of Brownian fibres, there is an elastic stress associated with the orientational diffusivity. Hinch & Leal (1972, 1976) derived the stress tensor, which is only a function of the second moment of the orientation vector a_{ij}:

$$\tau_{ij}^{elas} = \mu\phi F d a_{ij}. \tag{2.25}$$

They also derived the shape factor F for a spheroid in the limit of large aspect ratio:

$$F = \frac{3r_e^2}{\ln(2r_e) - \frac{1}{2}}. \tag{2.26}$$

The resulting form of the stress tensor used in our calculations is then given by:

$$\tau_{ij}^{f} = 2\mu\phi(2AE_{lk}a_{ijkl} + 2B(E_{ik}a_{kj} + E_{kj}a_{ik}) + CE_{ij} + Fda_{ij}). \tag{2.27}$$

As shown by Kim & Karrila (1991), the asymptotic forms of the shape factors are accurate for aspect ratios greater than 10.

2.4. *Semi-dilute concentration model*

The effect of increasing the concentration from the dilute to the semi-dilute regime on the dynamics described by Jeffrey's equation and on the fibre extra stress is a strong function of the rotary Péclet number, $Pe = \dot{\gamma}/d$, where $\dot{\gamma}$ is the characteristic shear or strain rate and d is the rotary diffusivity. If the Péclet number is small ($O(1)$), then the suspension is strongly Brownian and the resulting dynamics and stresses are described using the reptation model of Doi & Edwards (1986). We have not considered this model here.

In the non-Brownian limit ($Pe \to \infty$), the modifications to the dynamics and stress are far more modest. As shown by Koch & Shaqfeh (1990), the corrections to Jeffrey's equation in the semi-dilute regime due to fibre–fibre interactions are small (of order $\dot{\gamma}/\ln(1/\phi)$) and can be neglected to a first approximation. An alternative formulation for the case of semi-dilute non-Brownian fibres is the 'effective rotary diffusivity' of Folgar & Tucker (1984) in which $d = C\dot{\gamma}$ where C is an empirical interaction coefficient. Shaqfeh & Koch (1990) and Rahnama, Koch & Shaqfeh (1995) have shown that the effect of hydrodynamic interactions on this effective diffusivity in the semi-dilute regime is small. The most accurate estimation of this interaction coefficient has been derived using a rigorous analysis of hydrodynamic interactions by Koch (1995). Koch (1995) demonstrated that the resulting effective diffusivity should be an anisotropic tensor; as discussed in Larson (1999), the magnitude of the corresponding

interaction coefficient can be estimated using $C \approx 7.5 \times 10^{-4} nL^3/r_e \ln^2 r_e$. Using this expression with $r_e = 100$ and $nL^3 = 18$ gives an effective rotary Péclet number due to hydrodynamic interactions of approximately 100 000. Based on this estimate, we have neglected the effects of fibre–fibre interactions on the fibre rotational dynamics in the case of non-Brownian semi-dilute suspensions.

The stress tensor for non-Brownian semi-dilute suspensions is defined using the resistivity derived by Shaqfeh & Frederickson (1990), which rigorously accounts for many-body interactions:

$$\tau_{ij}^f = 2\mu\phi(2AE_{lk}a_{ijkl}), \tag{2.28}$$

where A is given by:

$$A = \frac{r_e^2}{4(\ln(1/\phi) + \ln(\ln(1/\phi)) + 1.439)}. \tag{2.29}$$

In the limit of large aspect ratio, the dilute stress scaling is dominated by the term proportional to A. The difference between the values of the shape factor A for high aspect ratio particles using the dilute and semi-dilute models is small, with the ratio of the values equal to 1.35 for $r_e = 100$ and $\phi = 0.015$.

2.5. *Non-dimensional form of the governing equations*

The governing equations are scaled using the centreline velocity U_c for velocity, the channel half-width h for length, the ratio h/U_c for time, $\rho(U_c)^2$ for pressure, and $(\mu U_c)/h$ for particle stress. The evolution of the fibre orientation moment tensor is given by:

$$\frac{\mathrm{D}a_{ij}}{\mathrm{D}t} = a_{ik}\frac{\partial u_j}{\partial x_k} + a_{kj}\frac{\partial u_i}{\partial x_k} + \frac{\beta - 1}{2}(E_{ik}a_{kj} + a_{ik}E_{kj}) - \beta E_{kl}a_{ijkl} + \frac{6}{Pe}\left(\frac{\delta_{ij}}{3} - a_{ij}\right), \tag{2.30}$$

where E_{ij} is twice the value in (2.7). The momentum equations with the fibre extra stress included are:

$$\frac{\partial u_i}{\partial t} + u_j\frac{\partial u_i}{\partial x_j} = -\frac{\partial P}{\partial x_i} + \frac{1}{Re}\frac{\partial^2 u_i}{\partial x_j \partial x_j} + \frac{\partial \tau_{ij}^f}{\partial x_j}, \tag{2.31}$$

or using the definition of the fibre stress tensor:

$$\begin{aligned}\frac{\partial u_i}{\partial t} + u_j\frac{\partial u_i}{\partial x_j} = &-\frac{\partial P}{\partial x_i} + \frac{1 + 2\phi}{Re}\frac{\partial^2 u_i}{\partial x_j \partial x_j} \\ &+ \frac{2\phi}{Re}\frac{\partial}{\partial x_j}[2AE_{lk}a_{ijkl} + 2B(E_{ik}a_{kj} + E_{kj}a_{ik})] + \frac{2F\phi}{Re\ Pe}\frac{\partial a_{ij}}{\partial x_j},\end{aligned} \tag{2.32}$$

in which the definition of the rate of strain tensor in (2.7) has been used.

In the equations above, the fourth moment a_{ijkl} is defined using either the IBOF or hybrid closure approximations as described in (2.15)–(2.20) or (2.12), respectively. The term $\partial \tau_{ij}^f/\partial x_j$ in (2.31) can be considered to be an additional body force due to the presence of the fibres. Note that the choice of the Newtonian viscosity for stress scaling means that an effective viscosity based on the suspension viscosity at the wall will be used in the definition of the turbulence viscous scaling. In this formulation, several fibre parameters need to be specified in addition to those required for the Newtonian case: the fibre aspect ratio r_e and the volume fraction ϕ, which can be related to the concentration parameter nL^3 by $\phi = (4\pi nL^3)/(3r_e^2)$ for the prolate spheroids considered here. For Brownian fibres, the rotary Péclet number $Pe = U_c/dh$

is specified and describes the strength of Brownian randomizations of orientation relative to a shear rate based on the centreline velocity and channel half-width. For the case of non-Brownian fibres, the terms proportional to Pe^{-1} are set equal to zero.

3. Numerical formulation

The flow solver used to perform the simulations presented here is based on a finite-difference channel-flow code that has been used for polymer drag reduction studies conducted at Stanford (Dubief 2002; Dubief *et al.* 2004). The computational domain is periodic in the streamwise and spanwise directions. Flow through the channel is maintained at a constant mass flow rate, such that drag reductions result in a pressure drop along the length of the channel. We first present details of the derivative formulation and solution algorithm, then discuss the selection of the simulation domain size and resolution.

3.1. *Spatial derivatives*

The flow solver uses energy-conserving second-order differences applied on a staggered grid. The fibre quantities a_{ij} and τ_{ij}^f are discretized at the cell centres (pressure nodes) using a fourth-order compact scheme as described by Min, Yoo & Choi (2001) in order to resolve better the small spatial scales associated with these terms. The advection terms of (2.30) are discretized using a third-order compact upwind scheme (Dubief *et al.* 2004*a*). This scheme is defined using an upwinding coefficient:

$$\varepsilon = \tfrac{1}{2}(s^- + s^+), \tag{3.1}$$

where s^- and s^+ are the sign of the velocity at the interface of the cell, the compact scheme is written as:

$$(2+3\varepsilon)\phi'_{i-1} + 8\phi'_i + (2-3\varepsilon)\phi'_{i+1} = \frac{6}{\Delta}\left[(-1-\varepsilon)\phi_{i-1} + 2\varepsilon\phi_i + (1-\varepsilon)\phi_{i+1}\right]. \tag{3.2}$$

Using this scheme, dispersion occurs at smaller scales than for the centred finite-difference scheme. The upwinding introduces numerical dissipation at small scales that stabilizes the solution of (2.30). However, as discussed by Min *et al.* (2001), an extra local dissipation is added wherever the tensor a_{ij} is not positive semi-definite, i.e. when $\det(a_{ij}) < 0$. The local dissipation is implemented using:

$$\frac{\partial a_{ij}}{\partial x_k} = \frac{\delta_u a_{ij}}{\delta x_k} + \begin{cases} 0 & \text{if } \det(a_{ij}) \geqslant 0, \\ \kappa \Delta_k^2 \dfrac{\delta_2^2 a_{ij}}{\delta^2 x_k} & \text{if } \det(a_{ij}) < 0. \end{cases} \tag{3.3}$$

The operators δ_u and δ_2 are the upwind-compact and second-order central differentiation schemes, respectively, Δ_k is the grid spacing in the x_k-directions, and κ is a constant set equal to 10. The selection of this constant is discussed in Dubief *et al.* (2004*a*) as well as in § 3.3.3, in which we examine the sensitivity of the results to the magnitude of this coefficient.

3.2. *Time-stepping technique*

The numerical method used to solve (2.32) is based on a semi-implicit fractional-step method (Le & Moin 1991). The Newtonian viscous stress in the wall-normal direction is advanced in time with the Crank–Nicolson scheme, while all other terms in (2.30) and (2.32) are advanced with a third-order Runge–Kutta (RK3) method. After

solving (2.30) at time (l), the resulting algorithm is

$$\frac{u_i^{(*)} - u_i^{(l-1)}}{\Delta t} = -\gamma_l N_i^{(l-1)} - \zeta_l N_i^{(l-2)} + \alpha_l \left(L_i^{(l)} + L_i^{(l-1)} + T_i^{(l)} + T_i^{(l-1)} \right), \tag{3.4}$$

$$\partial_k \partial_k \phi = \frac{1}{\alpha_l \Delta t} \partial_k u_k^{(*)}, \tag{3.5}$$

$$u_i^{(l)} = u_i^{(*)} - \alpha_l \Delta t \partial_i \phi. \tag{3.6}$$

In (3.4), $u_i^{(*)}$ are the intermediate velocity components not satisfying the continuity equation, ϕ is the first-order approximation to the pressure, and N, L and T represent finite-difference approximations (using the methods described in the previous section) to the viscous, convective and fibre stress terms, respectively:

$$N_i = \frac{\delta}{\delta x_k} u_i u_k, \tag{3.7}$$

$$L_i = \frac{1}{Re} \frac{\delta^2}{\delta x_k \delta x_k} u_i, \tag{3.8}$$

$$T_i = \frac{1}{Re} \frac{\delta}{\delta x_k} \tau_{ik}^f. \tag{3.9}$$

The index l denotes the RK3 substep and γ_l, ζ_l and α_l are the corresponding coefficients:

$$\gamma_1 = \tfrac{8}{15}; \quad \zeta_1 = 0; \qquad \alpha_1 = \tfrac{4}{15};$$
$$\gamma_2 = \tfrac{5}{12}; \quad \zeta_2 = -\tfrac{17}{60}; \quad \alpha_2 = \tfrac{1}{15};$$
$$\gamma_3 = \tfrac{3}{4}; \quad \zeta_3 = -\tfrac{5}{12}; \quad \alpha_3 = \tfrac{1}{6}.$$

Initial numerical results showed that the use of a fully explicit scheme for the time stepping of (2.30) is unstable for large values of *Pe*. For this reason, we implemented an implicit algorithm for time advancement of the orientation tensor evolution equation. The orientation tensor is iteratively solved using a trapezoid rule formulation at each velocity substep. We found that at large values of Péclet number, fibres would take on strongly anisotropic orientations with values of a single trace component approaching unity (complete alignment along a single axis) or zero (complete alignment in a plane). Using an explicit algorithm, it was possible for the fibres to 'overshoot' the full alignment condition, resulting in loss of positive definiteness. To correct this problem, negative values of the trace components of the orientation tensor were clipped, and then the corrected values were used for additional iterations, ensuring that the off-diagonal values were also corrected. These clipping corrections were typically less than 0.1% of the value of the orientation tensor.

Following the same numerical scheme as for the momentum equations (2.32), the time advancement of (2.30) is

$$\frac{a_{ij}^{(l)} - a_{ij}^{(l-1)}}{\Delta t} = \alpha_l \left(R_{ij}^{(l)} + R_{ij}^{(l-1)} \right), \tag{3.10}$$

where,

$$R_{ij}^{(l)} = -u_k^{(l-1)} \partial_k a_{ij}^{(l)} + a_{ik}^{(l)} \partial_k u_j^{(l-1)} + a_{kj}^{(l)} \partial_k u_i^{(l-1)} + \frac{\beta - 1}{2} \left(E_{ik}^{(l-1)} a_{kj}^{(l)} + a_{ik}^{(l)} E_{kj}^{(l-1)} \right)$$
$$- \beta a_{ijkl}^{(l)} E_{kl}^{(l-1)} + \frac{6}{Pe} \left(\frac{\delta_{ij}}{3} - a_{ij}^{(l)} \right) \tag{3.11}$$

Mesh	Δ_x^+	Δ_y^+	Δ_z^+
$64 \times 129 \times 32$	15	$0.325 \rightarrow 5.9$	9.0
$64 \times 129 \times 64$	15	$0.325 \rightarrow 5.9$	4.5
$80 \times 141 \times 80$	12.5	$0.3 \rightarrow 5.4$	3.75
$96 \times 151 \times 96$	10	$0.27 \rightarrow 10$	3.1

TABLE 1. Summary of meshes considered for grid resolution study. Spacings are based on viscous length of Newtonian turbulent flow.

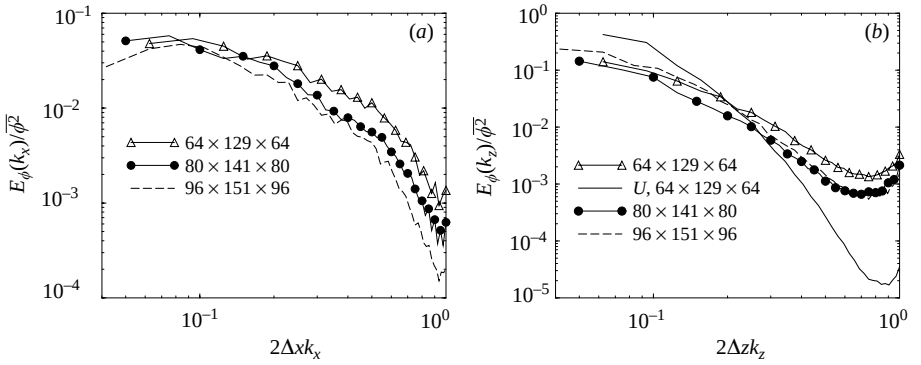

FIGURE 1. Power spectra in (*a*) x and (*b*) z of fibre stress τ_{12} as a function of mesh resolution. Spectra of velocity are also shown for the spanwise case. Spectra are normalized by their respective variances.

and

$$R_{ij}^{(l-1)} = -u_k^{(l-1)}\partial_k a_{ij}^{(l-1)} + a_{ik}^{(l-1)}\partial_k u_j^{(l-1)} + a_{kj}^{(l-1)}\partial_k u_i^{(l-1)} + \frac{\beta-1}{2}\left(E_{ik}^{(l-1)}a_{kj}^{(l-1)} + a_{ik}^{(l-1)}E_{kj}^{(l-1)}\right) - \beta a_{ijkl}^{(l-1)}E_{kl}^{(l-1)} + \frac{6}{Pe}\left(\frac{\delta_{ij}}{3} - a_{ij}^{(l-1)}\right). \tag{3.12}$$

3.3. *Grid resolution and domain size*

We have performed both mesh refinement and box size studies. For both of these studies, the starting flow field is a Newtonian turbulent flow with a Reynolds number of 7500 based on the centreline velocity and channel half-width. The effect of the fibre stresses are included in the flow solution. We have considered fibres with an aspect ratio of 100 and $nL^3 = 18$. For the grid resolution study, a 'minimal channel' (Jimenez & Moin 1991) of dimensions $\pi h \times 2h \times h$ was used with grid resolutions described in table 1. We considered three meshes of increasing resolution in all dimensions as well as one coarse mesh for potential use in exploring the effect of rheological parameters. For the box size study, we have considered a minimal channel with resolution $64 \times 129 \times 64$ and a double minimal channel in the x and z dimensions with resolution $128 \times 129 \times 128$. For the Newtonian flow, $h^+ = 300$.

3.3.1. *Grid resolution*

The power spectra of the fibre shear stress in the streamwise and spanwise directions are shown in figure 1. We obtain approximately two decades of decay for the fibre stress τ_{12}, which is adequate, but not nearly as good as that for the velocity. The

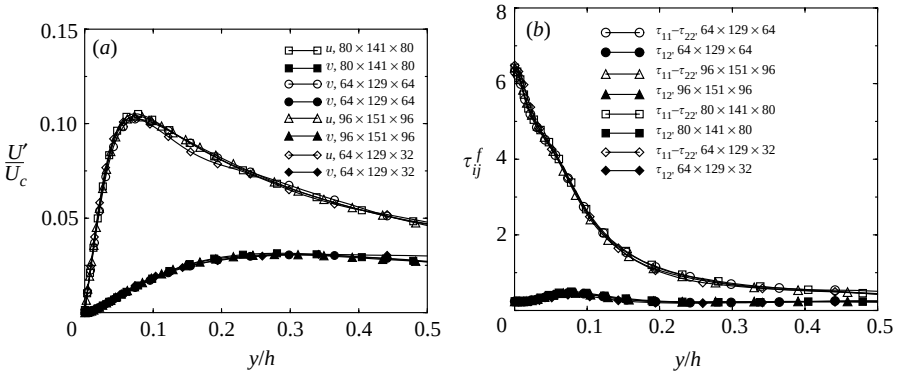

FIGURE 2. Effect of mesh resolution on (*a*) r.m.s. velocity fluctuations and (*b*) mean fibre stresses.

other fibre stress components have similar behaviour with the most slowly decaying component, τ_{22}, having approximately one-half decade less decay. The improvement in spectral decays going from the medium to the fine mesh is modest in both the x- and z-directions.

The slow decay of the stress components, even for the finest meshes investigated, indicate that the smallest scales of the fibre stresses are not well resolved. This behaviour is a result of the character of the orientation tensor evolution equation (2.30) and the structure of near-wall turbulence. The evolution equation for the orientation tensor a_{ij} contains no diffusive terms and the only term containing a spatial derivative of a_{ij} is the advection term. If we consider the evolution of the suspension structure in near-wall turbulence, near-wall vortices contain regions of sharp variation in velocity gradient, ranging from pure rotation at the vortex core to extensional flow between vortices. These strong spatial gradients in flow combined with the lack of spatial diffusion of a_{ij} generate sharp gradients in the orientation tensor. This behaviour will be most pronounced for non-Brownian fibres since the disordering term in (2.30) is proportional to Pe^{-1}. As discussed in Batchelor (1959) in the context of passive scalars and in Dubief *et al.* (2004*a*) in the context of flexible polymer additives, advection in combination with low diffusivity is known to create spatial scales of concentration variation much smaller than the flow dissipative scale. This analogy to passive scalars suggests that full resolution of the fibre stresses will require resolution of scales smaller than the Kolmogorov scale. This degree of resolution is not possible with current computational resources.

Selected flow statistics as a function of grid resolution are presented in figure 2. The r.m.s. of the velocity fluctuations and the mean fibre stresses are nearly identical, even for the coarsest resolution ($64 \times 129 \times 32$) considered. The differences between the results obtained using the $80 \times 141 \times 80$ and $96 \times 151 \times 96$ meshes are also modest. Although this analysis does not rigorously demonstrate the grid independence of our results, extrapolating from the modest variations over the limited range of resolutions considered here we anticipate that results obtained using higher resolutions will be not be qualitatively different. Based on these results, the coarse mesh appears to be adequate for capturing qualitative trends and this resolution was used for a parametric study of the effect of fibre concentration and rotary Péclet number on drag reduction. Based on both the spectra and the statistics, the $80 \times 141 \times 80$ grid was chosen as the best tradeoff between accuracy and computational cost.

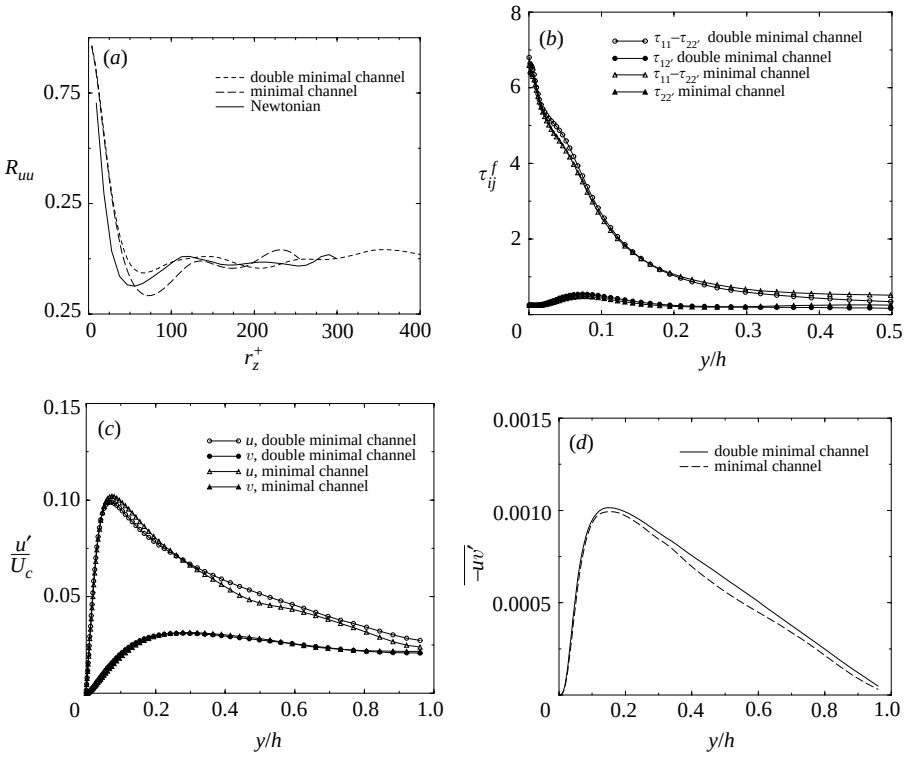

FIGURE 3. Effect of simulation domain size on selected flow statistics. (*a*) Two-point spanwise correlation of the streamwise velocity fluctuation at $y^+ \approx 10$. (*b*) Mean fibre stresses as function of wall-normal position. (*c*) Reynolds stress normalized using outer variables. (*d*) Root mean square of velocity fluctuations scaled with outer variables.

3.3.2. *Simulation domain size*

The minimal channel was developed by Jimenez & Moin (1991) to study near-wall turbulence and consists of the smallest periodic box in the streamwise and spanwise direction that is required to obtain a self-sustaining turbulent flow. They showed that the minimal channel accurately captures the near-wall statistics of turbulent channel flow. For the case of a drag-reduced flow, the spatial scales of the turbulence are increased and thus it is unclear if the box size associated with a Newtonian minimal channel flow is adequate. The inability to capture these large scales has been shown by Dubief *et al.* (2004*b*) to give rise to numerical artefacts in simulating drag-reduced flows that disappear when using a large box.

We quantify the effect of box size on fibre and flow quantities shown in figure 3. The two-point spanwise velocity correlation can be used to determine spatial structures in the flow domain as discussed in Kim, Moin & Moser (1987). At the low Reynolds numbers considered here, the mean streak spacing is approximately twice the separation distance of the negative minimum of the spanwise correlation. At $y^+ \approx 10$, considered here, the streaks are most pronounced. The Newtonian two-point correlation shows a minimum at 50 wall units, corresponding to a streak spacing of 100, consistent with the results of Choi *et al.* (1994) and Jimenez & Moin (1991). The minimal channel has a much stronger correlation than both the Newtonian and double minimal channel flow, suggesting that the streaky structures are more

κ	Nodes affected	Drag reduction (%)
1.0	$\sim$ 4–5%	22
10.0	$\sim$ 0.5–1.0%	18.5
100.0	$\sim$ 0.1%	14

TABLE 2. Effect of LAD coefficient, κ on drag reduction. Hybrid closure, $Pe = 1000$, $\phi = 0.0075$ and $r_e = 100$. Drag reduction is defined in § 4.1.

pronounced in the minimal channel than in either of the other cases. The turbulence intensities, mean velocities and mean fibre stresses are all quantitatively similar in the near-wall region where fibre interactions will be shown to be most important. We have also examined the correlations presented in § 5 using both domains and have found no significant differences. Based on these similarities and the large computational costs associated with using the double channel, we have chosen to use the minimal channel for this study and anticipate that the effects of using a significantly larger domain will be modest.

3.3.3. *Local artificial dissipation*

An additional concern addressed by an analysis of the stress spectra is the impact of the local dissipation scheme on the accuracy of the fibre stresses. Some amount of either local or global artificial diffusion is necessary to obtain numerically stable solutions as demonstrated by Sureshkumar *et al.* (1997) and Min *et al.* (2001) for polymer-induced drag reduction. As previously discussed, we have used local artificial diffusion in the treatment of the advection of the fibre orientation tensor; when the determinant of the orientation tensor is negative, an extra artificial diffusion term is added to the advection term. If this additional term is too large, the resulting stresses will be too dispersed and the results inaccurate. Alternatively, as discussed in Dubief *et al.* (2004*a*), the combination of the compact upwind scheme and LAD can be considered to be a MILES (monotone integrated large eddy scheme) subgrid scale model for polymer or fibre stress. As discussed in § 3.3.1, the fibre quantities are characterized by small subgrid scale spatial variations and are therefore affected by the choice of LAD coefficient.

We have completed a basic characterization of the effect of the LAD coefficient, κ, on the results as summarized in table 2 using the $64 \times 129 \times 32$ mesh and fibres with $Pe = 1000$ and $nL^3 = 18$ using three different values of the coefficient differing by one order of magnitude. Increasing the LAD coefficient decreases both the number of nodes affected and the degree of drag reduction. In figure 4, we show that the r.m.s. fluctuations in the stress are decreased as the LAD coefficient is increased, which is consistent with the drag reduction behaviour reported in table 2. We will show that large stress fluctuations are correlated with drag reduction in § 5. The power spectra of fibre shear stress for the three values of the LAD coefficient considered are presented in figure 4 and show little variation in the degree of decay, at least for this mesh and parameter set. If the LAD coefficient is increased by too much, the diffusion term in (3.3) becomes larger than the advection term and limits the time step. This behaviour would manifest itself as artefacts at high wavenumbers in the power spectra. These are not observed for the case of $\kappa = 100$. We found that the case of $\kappa = 1$ eventually became unstable for $Pe = 1000$ at long times and was not stable for non-Brownian fibres. These results, combined with the fact that we see substantial drag reduction over two orders of magnitude of the LAD coefficient, suggest that the qualitative

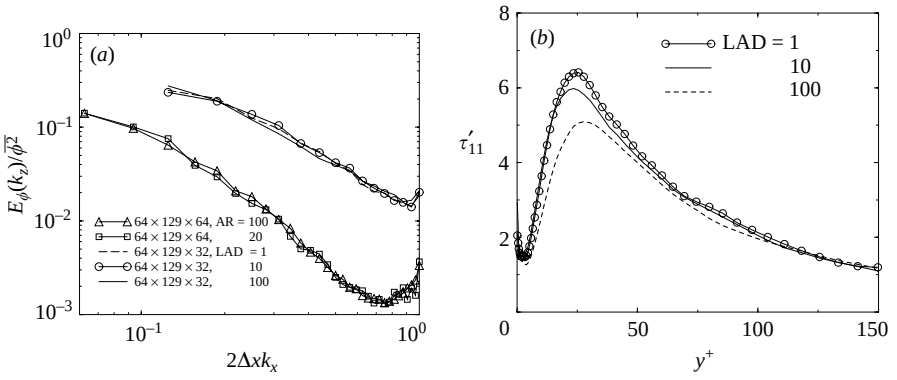

FIGURE 4. Effect of variation of local artificial dissipation coefficient. (*a*) Power spectra in z of fibre stress τ_{12} and (*b*) r.m.s. fluctuations of fibre stress component τ_{11} as function of LAD coefficient. Spectra are normalized by their respective variances. Fibre parameters: $Pe = 100$, $nL^3 = 18$. Grid resolution for stresses: $64 \times 129 \times 32$.

results are not impacted by our choice of κ, but the variations suggest that lower values are better. An LAD coefficient of 10 gave robust performance for all values of the rotary Péclet number and aspect ratio, but this choice of coefficient was not optimized. Since we lack exact solutions for the Fokker–Planck equation for a fully coupled simulation in order to determine the impact on the numerical solution, we used $\kappa = 10$ in order to obtain numerically stable solutions for the parameter range of interest.

We have also considered the effect of the fibre properties on the number of nodes affected by LAD. By reducing the aspect ratio, the fibre stresses are dispersed at the smallest scales owing to the decreased ability of the fibres to align along streamlines. As a result, less artificial diffusion is necessary. For an aspect ratio of 20, local artificial diffusion is required at less than 0.001% of the nodes. As seen in figure 4, the power spectrum of fibre stress for this case is not appreciably different than that for fibres with an aspect ratio of 100 – a calculation where roughly 1000 times more nodes are affected by LAD. In this case, a physical dissipation eliminates the need for application of the artificial dissipation. Decreasing the rotary Péclet number also decreases the degree of alignment and has an effect similar to the reduction of aspect ratio.

3.3.4. *Time averaging and initial conditions*

Based on the results of the above studies, we present results using two grid resolutions in the minimal channel flow. For our parametric study of the effect of rheological parameters in § 6, we used the coarsest mesh described above. For the calculation of turbulence statistics and our mechanistic studies we used the $80 \times 141 \times 80$ mesh. In all simulations, the local artificial dissipation coefficient κ was equal to 10. A statistically converged turbulent Newtonian flow with $Re = 7500$ was used for the initial velocity field in all simulations unless stated otherwise. An isotropic initial fibre orientation was used ($a_{ij} = \delta_{ij}/3$). Because of this initial condition, the flow undergoes a transient lasting approximately 25 time units. Upon reaching a statistically steady state at approximately 50 time units, statistics were collected over a minimum of 200 time units thereafter. We have used the IBOF closure for the results presented in the following two sections and the hybrid closure for § 6 unless otherwise noted.

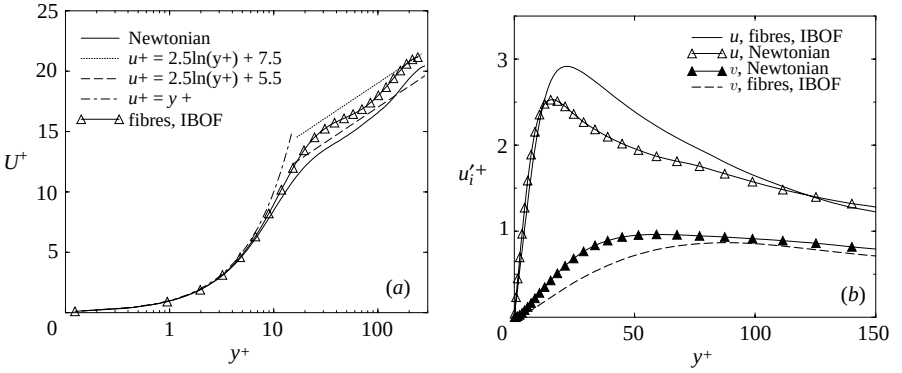

FIGURE 5. (*a*) Mean velocity and (*b*) r.m.s. velocity fluctuations scaled with friction velocity. Fibre parameters: $Pe = 1000$, aspect ratio = 100, $nL^3 = 18$.

4. Turbulence statistics and structure

In this section, we present results for the case of Brownian fibres with $Pe = 1000$, aspect ratio of 100 and concentration $nL^3 = 18$, using the IBOF closure. For this case, we achieved a drag reduction of 13.4%, defined relative to the Newtonian friction velocity at the effective Reynolds number based on the total suspension viscosity:

$$\%DR = 1 - \left(\frac{u_\tau^F}{u_{\tau, Re_{eff}}^N} \right)^2 \times 100, \tag{4.1}$$

where the non-dimensional friction velocity for the fibre suspensions is defined using the total average shear stress at the wall:

$$\frac{u_\tau^F}{U} = \sqrt{\frac{\mathrm{d}\overline{U}/\mathrm{d}y_{wall} + \overline{\tau_{xy,wall}^F}}{Re}} \tag{4.2}$$

and the effective Reynolds number, Re_{eff} is defined using the effective viscosity of the suspension at the wall:

$$\mu_{eff} = 1 + \frac{\overline{\tau_{xy,wall}^F}}{\mathrm{d}\overline{U}/\mathrm{d}y_{wall}}. \tag{4.3}$$

All results presented using viscous units are scaled using μ_{eff}. This rescaling is equivalent to that used by Beris and coworkers (Sureshkumar *et al.* 1997; Dimitropoulos *et al.* 1998) for polymeric drag reduction. For the Péclet number of 1000 considered here, the effective Reynolds number is 6710.

4.1. *Velocity statistics*

The mean velocity and r.m.s. velocity fluctuations for the Newtonian and drag-reduced cases are presented in figure 5. The fibre drag-reduced mean velocity profile is similar to that observed in other drag-reduced flows (Choi *et al.* 1994; Sureshkumar *et al.* 1997): the slope of the log-law region is roughly the same as that of the Newtonian case, but the intercept with the linear region ($u^+ = y^+$) is shifted upwards. This log-law shift is indicative of a thickening of the viscous sublayer. The r.m.s. velocity fluctuations are also qualitatively similar to those seen in polymeric simulations, with an increase and outward shift of the streamwise intensity and a decrease in the wall-normal and spanwise fluctuations.

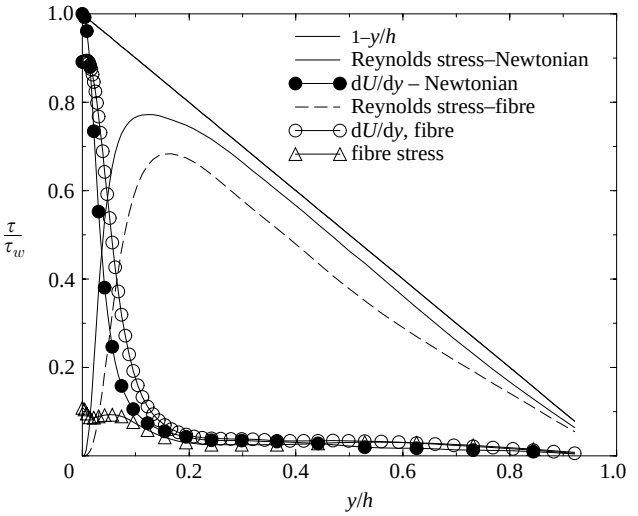

FIGURE 6. Stress balance for fibres. Fibre parameters: $Pe = 1000$, aspect ratio $= 100$, $nL^3 = 18$.

Figure 6 shows the contributions to the mean shear stress as a function of distance from the wall. The stress balance is given by:

$$-\frac{\overline{uv}}{u_\tau^2} - \left(1 - \frac{y}{h}\right) + \frac{1}{u_\tau^2 Re}\frac{\mathrm{d}\overline{U}}{\mathrm{d}y} + \frac{1}{u_\tau^2 Re}\overline{\tau_{xy}^f} = 0. \tag{4.4}$$

In (4.4), the Reynolds stresses are given by $\overline{uv}/u_\tau^2$, the Newtonian viscous stress by $1/(u_\tau^2 Re)\mathrm{d}U/\mathrm{d}y$ and the mean fibre shear stress by $1/(u_\tau^2 Re)\tau_{xy}^f$. Again, we see qualitative agreement with results obtained using flexible polymer models. Reynolds stresses are decreased relative to the Newtonian case throughout the entire channel. This suggests that the fibres most strongly affect the flow in the region $y^+ < 100$, or the near-wall region where vortex structures are most pronounced. The average fibre shear stresses show a maximum value at the wall and large shear stress in the buffer region ($y/h < 0.15$).

The turbulent kinetic energy balance for the case of viscoelastic additives has been formulated by Dimitropoulos *et al.* (2001). The turbulent kinetic energy is obtained from the Reynolds stress budget:

$$\frac{\partial \overline{u_i u_j}}{\partial t} + U_k \frac{\partial \overline{u_i u_j}}{\partial t} = P_{ij} + Q_{ij}^N + Q_{ij}^F + D_{ij} + \Pi_{ij} + \epsilon_{ij}^N + \epsilon_{ij}^F. \tag{4.5}$$

The turbulent kinetic energy is recovered by setting $i = j$, summing over the index i, and dividing by 2. The terms in the balance are defined as follows:

$$P_{ij} = -\left(\overline{u_i u_k}\frac{\partial U_j}{\partial x_k} + \overline{u_j u_k}\frac{\partial U_i}{\partial x_k}\right) \tag{4.6}$$

is the production rate of Reynolds stress;

$$Q_{ij}^N = -\frac{\partial \overline{u_i u_j u_k}}{\partial x_k} \tag{4.7}$$

is the Newtonian transport of Reynolds stress;

$$D_{ij} = \frac{\partial^2(\overline{u_i u_j})}{\partial x_k \partial x_k} \tag{4.8}$$

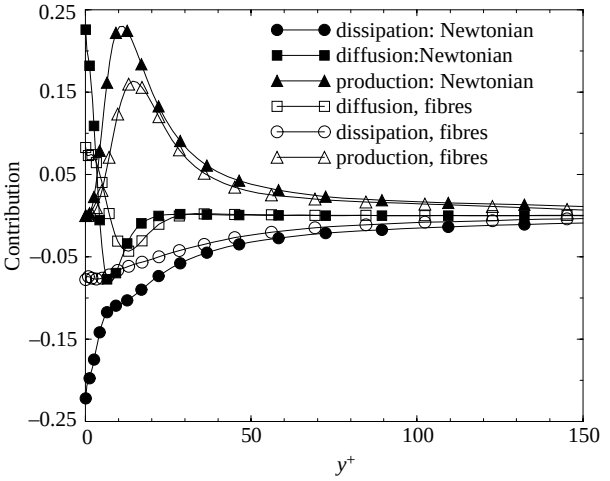

FIGURE 7. Turbulent kinetic energy profiles: comparison of Newtonian and fibre drag-reduced profiles: dissipation, diffusion and production contributions. Fibre parameters: $Pe = 1000$, aspect ratio $= 100$, $nL^3 = 18$.

is the diffusion of the Reynolds stress;

$$\Pi_{ij} = -\overline{\left(u_i \frac{\partial p}{\partial x_j} + u_j \frac{\partial p}{\partial x_i}\right)} \tag{4.9}$$

is the velocity–pressure gradient term; and

$$\epsilon_{ij}^N = -2\overline{\frac{\partial u_i}{\partial x_k}\frac{\partial u_j}{\partial x_k}} \tag{4.10}$$

is the direct viscous dissipation of the Reynolds stress. There are two additional terms in the kinetic energy balance that result from the presence of fibre stresses:

$$Q_{ij}^F = -\frac{\partial\left(\overline{u_i \tau_{jk}^f + u_j \tau_{ik}^f}\right)}{\partial x_k}, \tag{4.11}$$

which is turbulent transport resulting from fluctuating fibre stress; and

$$\epsilon_{ij}^F = -\overline{\frac{\partial u_i}{\partial x_k}\tau_{jk}^f + \frac{\partial u_j}{\partial x_k}\tau_{ik}^f}, \tag{4.12}$$

which is an additional dissipation due to fluctuations in fibre stresses. As explained by Dimitropoulos *et al.* (2001) this term can also be viewed as a coupling between the velocity gradient and the fibre stress. As in the polymeric case, we have found that these two contributions to the energy budget are small and define a total fibre contribution to the budget as the sum of (4.11) and (4.12).

As seen in figure 7, the addition of fibres primarily affects the production, diffusion and dissipation terms of the kinetic energy balance. Fibres appear to act in a manner similar to flexible polymers, reducing the production of turbulent kinetic energy and acting as an additional source of dissipation. There is also a shift of the maxima and minima away from the wall which is consistent with the larger buffer layer characteristic of a drag-reduced flow. The total fibre contribution is of the same order as the velocity–pressure gradient and dissipation terms as seen in figure 8. In the case of polymer-induced drag reduction, the additive contribution is a weak sink in most

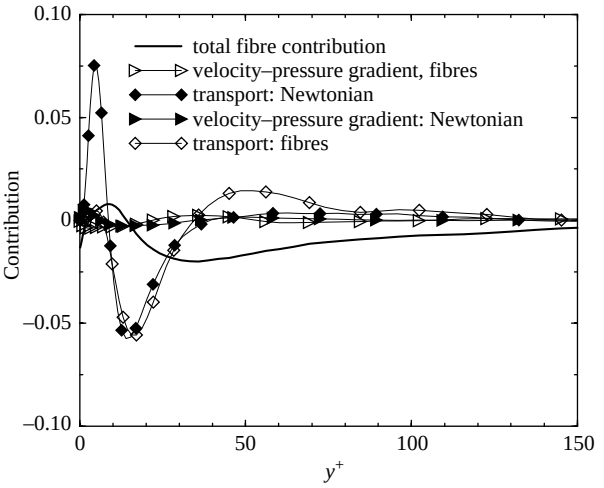

FIGURE 8. Turbulent kinetic energy profiles: comparison of Newtonian and fibre drag-reduced profiles: transport, velocity-pressure gradient and fibre contributions. Fibre parameters: $Pe = 1000$, aspect ratio $= 100$, $nL^3 = 18$.

of the channel except near the walls, where the polymeric stresses act as a source term (Dimitropoulos *et al.* 2001). We see similar behaviour in the case of rigid fibres, with a small positive contribution near the walls and a strong negative contribution in the buffer region between $y^+ = 25$ and $y^+ = 50$.

As in the polymer case, this positive contribution can be attributed to large fluctuations in the streamwise velocity in the region between $y^+ = 10$ and $y^+ = 25$ that act to stretch (in the case of flexible polymers) or more strongly orient (fibres) in the x-direction than the mean shear in the viscous sublayer below $y^+ = 10$. The resulting maximum in stress around $y^+ \simeq 20$, corresponding to the location of the maximum streamwise velocity fluctuations, is visible in the shapes of the mean stress profiles for the IBOF closure in figure 22. For $y^+ < 20$, both the turbulent transport and dissipation terms related to the fibre stress positively contribute to the TKE budget.

4.2. *Turbulence structure*

The r.m.s. fluctuations of the streamwise vorticity for both the Newtonian and fibre cases are shown in figure 9. As discussed in Kim *et al.* (1987) and Sureshkumar *et al.* (1997), the minima and maxima of the profiles correspond to the average locations of the edges and centres of the near-wall vortex structures. The decrease in the vorticity fluctuations, as well as the broadening of the peak, suggests an increase in the size and weakening of the near-wall vortex structures. Alternatively, the decrease in the magnitude of the vorticity fluctuations suggests that the sweep motion associated with the streamwise vortices in the fibre case is not as effective as that of the Newtonian case in creating a high wall shear stress region as discussed by Kravchenko *et al.* (1993). To illustrate more clearly the effect of the fibres on the near-wall vortices, in figure 10 we show instantaneous visualizations of the vortices. The vortices are visualized using iso-Q surfaces as discussed in Dubief & Delcayre (2000), where Q is the second invariant of the velocity gradient tensor (Blackburn, Mansour & Cantwell 1996). For positive values of Q, the local rotation rate exceeds the strain rate and has been shown to correlate with vortex structures by both Blackburn *et al.* (1996) and Dubief & Delcayre (2000). We have chosen a value of $Q = 1.0$ for the Newtonian flow

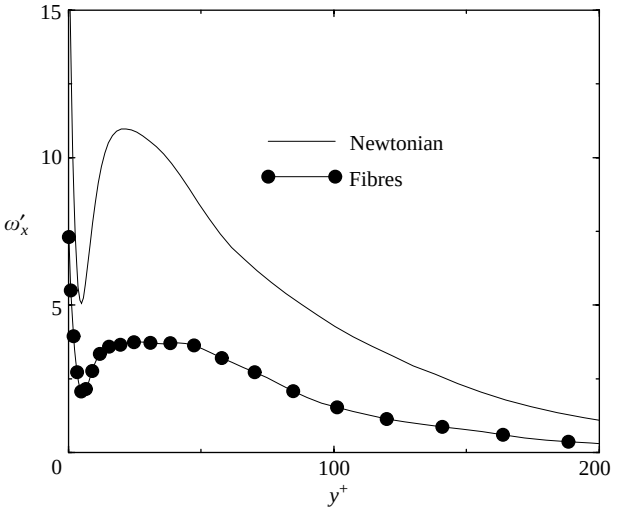

FIGURE 9. Effect of fibres on r.m.s. of streamwise vorticity fluctuations. Fibre parameters: $Pe = 1000$, $nL^3 = 18$, $r_e = 100$.

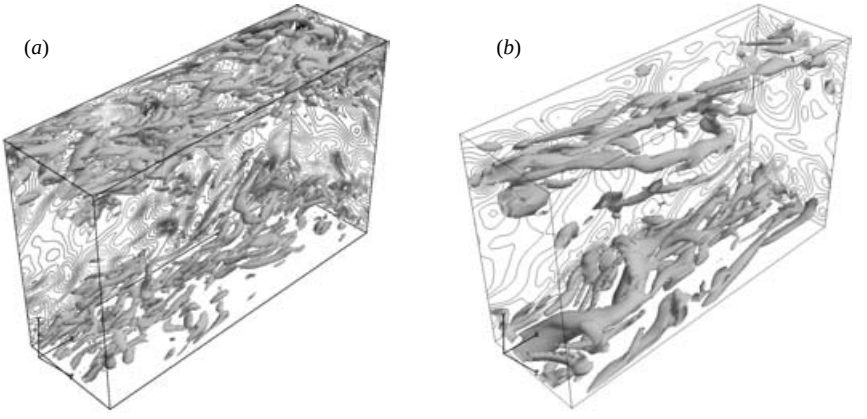

FIGURE 10. Instantaneous visualizations of near-wall vortex structures and contours of wall-normal velocity. (*a*) Newtonian. (*b*) Fibres with $Pe = 1000$, aspect ratio $= 100$, and $nL^3 = 18$. Contours of velocity are equally spaced and defined from $-0.013U_c$ to $0.013U_c$.

and $Q = 0.3$ for the fibre flow, based on values chosen by Dubief & Lele (2001) for visualization of a polymeric flow exhibiting comparable drag reduction. The vortices are both larger and weaker, and the contours of the wall-normal velocity show an increase in spacing in the fibre flow. The vortices are also spread out over a larger region in the wall-normal direction relative to the Newtonian flow.

Since the near-wall vortices are affected by the fibres, we also expect the structure of the near-wall streaks to be modified. We present instantaneous visualizations of the streaks in figure 11 at $y^+ \approx 10$. These visualizations show that the alternating regions of high- and low-speed flow are increased in scale by the addition of fibres. Alternative evidence for this increase in streak spacing was shown using the velocity autocorrelation in the previous section. The streak spacing is increased from approximately 100 wall units in the Newtonian case to 150 wall units in the fibre case using the effective friction velocity.

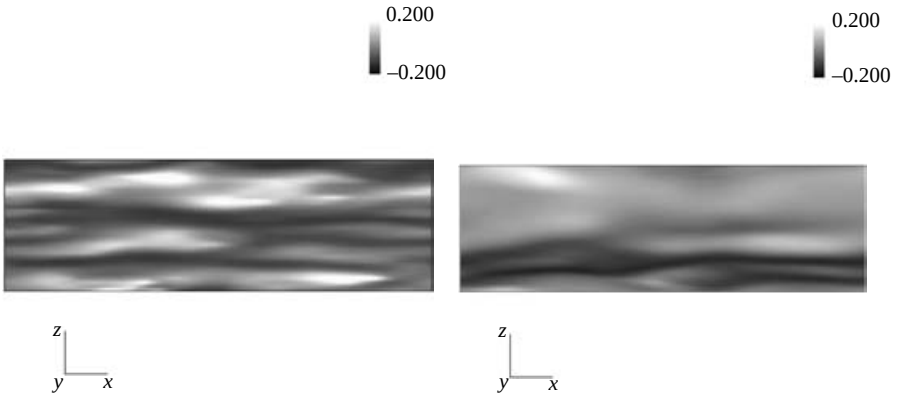

FIGURE 11. Instantaneous visualizations of near-wall streaks. (*a*) Newtonian. (*b*) Fibres with $Pe = 1000$, aspect ratio $= 100$, and $nL^3 = 18$. Note increase in scale of dark (low speed) and white (high speed) regions in fibre case.

5. Mechanisms for drag reduction

In this section, we will use a combination of statistical analysis, flow visualizations and numerical experiments to explain the process by which fibres cause turbulent drag reduction. We begin by considering the PDFs of fibre stresses with various flow and fibre quantities. Asymmetries in the PDFs indicate that correlations exist between the fibre stress and the flow or fibre quantity, and the colour is indicative of the probability with darker being more probable. We present the PDFs of the fibre normal stress τ_{22} and various quantities in figure 12. Large values of the fibre normal stress are correlated to low values of v' and w', suggesting that large stresses exist in stagnation regions. The diagonal components of the velocity gradient tensor associated with extension are also associated with large stresses, and for the component τ_{22}, they are correlated with an extensional flow with principal line stretching in the y-direction (positive $\partial v/\partial y$ and negative $\partial u/\partial x$ and $\partial w/\partial z$). An alternative way to express this correlation is to consider the relationship between τ_{22} and the quantity $\%E$ defined as:

$$\%E = \frac{(E_{ij}E_{ij})^{0.5}}{(E_{ij}E_{ij})^{0.5} + (\Omega_{ij}\Omega_{ij})^{0.5}}, \tag{5.1}$$

which is clearly a measure of the amount of pure straining motion in the flow. This quantity is equal to 0.5 in simple shear and 1 in pure extension. As shown in figure 12, large values of τ_{22} correlated with values of $\%E$ greater than 0.5. We see similar correlations for the fibre normal stress τ_{33} (not shown). The fibre stress is also correlated to values of the orientation tensor, with large values of τ_{22} correlated with values of a_{22} approaching unity, suggesting that the large values of stress are due to particles that are largely aligned with the y-axis. Large values of τ_{33} are associated with values of a_{33} approaching unity, suggesting that the largest values of this stress component are generated when fibres are almost completely aligned in the z-direction. The PDFs also show that large stress events are generally rare events, with the largest stresses occurring in only 0.001% of the observations.

The aforementioned observations regarding the relationships of the diagonal values of the velocity gradient tensor and the amount of straining motion in the flow to the fibre stress are strictly only valid for two-dimensional flows. To determine more rigorously the relationship between fibre normal stress and the flow kinematics in the

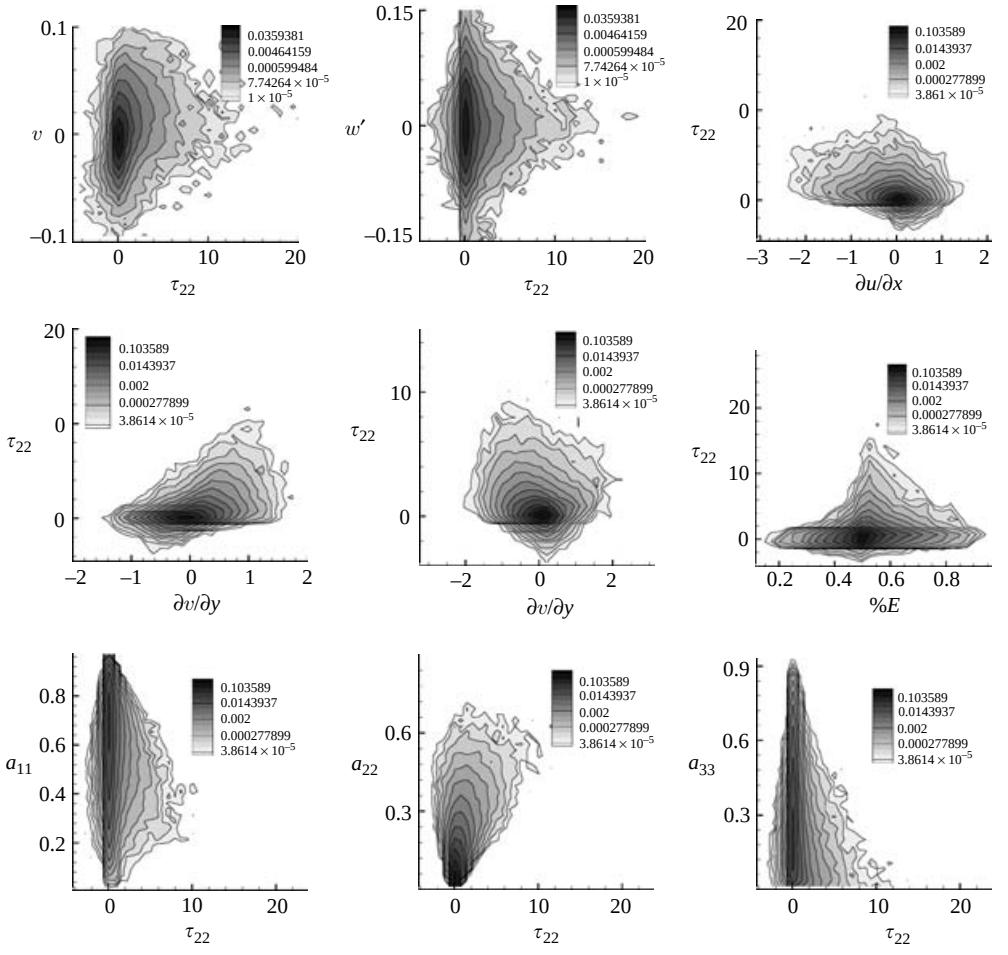

FIGURE 12. Correlations (PDF's) of fibre normal stress, τ_{22}, with various flow and fibre quantities. Top row, left to right: τ_{22} vs. v', τ_{22} vs. w', τ_{22} vs. $\partial u/\partial x$; middle row, left to right: τ_{22} vs. $\partial v/\partial y$,τ_{22} vs. $\partial v/\partial z$, τ_{22} vs. $\%E$; bottom row, left to right: τ_{22} vs. a_{11}, τ_{22} vs. a_{22}, τ_{22} vs. a_{33}.

three-dimensional flows of interest here, we adopt the analysis of Blackburn *et al.* (1996). We consider a contour plot of fibre normal stress versus Q and R, where Q and R are defined as

$$Q = \tfrac{1}{2}\left([\mathrm{tr}(A_{ij})]^2 - \mathrm{tr}\left[A_{ij}^2\right]\right), \tag{5.2}$$

$$R = -\det(A_{ij}), \tag{5.3}$$

where A_{ij} is the velocity gradient tensor. The discriminant

$$D = (27/4)R^2 + Q^3 = 0 \tag{5.4}$$

defines the transition between rotational and extensional flows. For flows with $D < 0$, the flow is extensional. In figure 13 we show the contours of τ_{22} and τ_{33} versus Q and R at $y^+ = 30$. Large stresses are correlated with regions of negative Q and positive R below the $D = 0$ line. To explain the importance of this region of Q-R space, we consider the PDF of Q versus R at $y^+ = 30$ for the fibre drag-reduced flow and

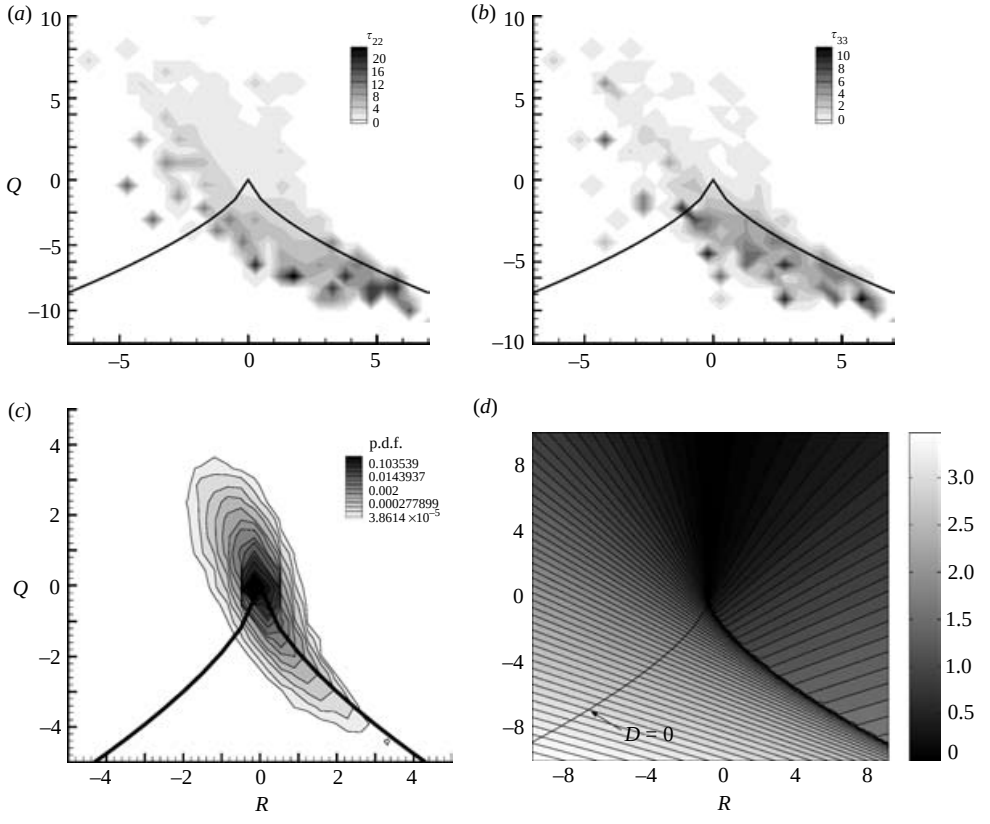

FIGURE 13. Distributions of fibre stresses with respect to invariants of velocity gradient tensor Q and R. Regions below the $D=0$ line (black cusp) are extensional flow. (*a*) τ_{22}, (*b*) τ_{33}. (*c*) PDF of Q *vs.* R for fibre drag-reduced flow. (*d*) Contours of maximum real part of eigenvalues of velocity gradient tensor.

a contour plot of the maximum of the real part of the eigenvalues of the velocity gradient tensor as shown in figures 13(*c*) and 13(*d*), respectively. The highest fibre stresses are associated with regions of Q-R space having the largest maximum real part of the eigenvalue with a finite probability of occurring in the flow. These regions in Q-R space are associated with the strongest extensional flows, and since the largest stresses are clustered near the $D=0$ line in the bottom right quadrant, these are predominantly biaxial extensional flows. It is remarkable that the regions of large fibre stress, and thus the primary action of the fibres on the flow, are associated with $Q<0$, $R>0$ flows that have exceedingly low probability and are located in the inter-vortex regions (Terrapon *et al.* 2004). These rare flow events appear to be critical to the drag-reduction effectiveness of the fibres. Recent work performed at Stanford has demonstrated that these flows are also important in the onset of polymer-induced drag reduction; see Terrapon *et al.* (2004) for a full discussion of this topic.

To correlate fibre stresses to drag reduction, we consider the viscoelastic momentum equation (2.32). Gradients in τ_{22} can generate a body force that, if opposite in sign to v', acts to decrease the fluctuations in this velocity component. A similar relationship holds for τ_{33} and w'. Decreases in the fluctuations of v' and w' are one of the indicators of drag reduction. We consider the scalar product of the divergence of the

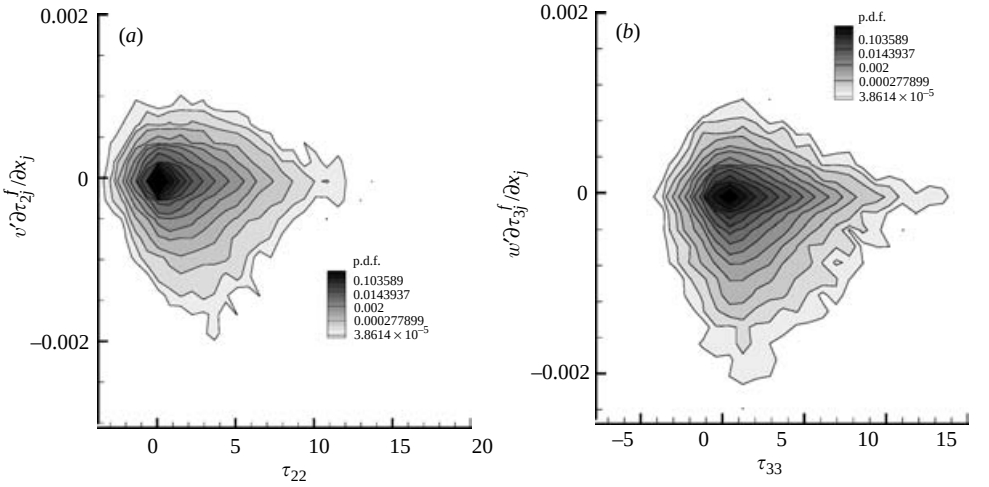

FIGURE 14. Correlations of fibre stresses with scalar product of fluctuation velocity and fibre body force or 'fibre work'. (*a*) τ_{22} *vs.* $v'\partial_j\tau_{2j}$. (*b*) τ_{33} *vs.* $w'\partial_j\tau_{3j}$.

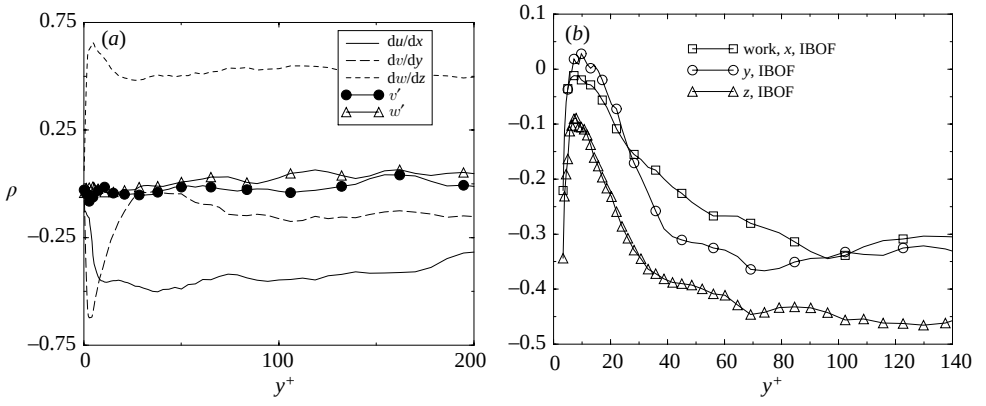

FIGURE 15. Single-point correlations *vs.* y^+. (*a*) Fibre stress τ_{33} and various flow quantities. (*b*) Fibre work and fluctuation velocities in specified direction.

stress and the relevant velocity component as a measure of these decelerations, with a negative product being indicative of a drag reduction effect. We will refer to this product as 'fibre work'. In figure 14, it can be seen that the negative values of the scalar product $v'\partial\tau_{2j}/\partial x_j$ are correlated with moderate values of τ_{22}. We also show in figure 14 a similar correlation for $w'\partial\tau_{3j}/\partial x_j$ and τ_{33}. Since the body forces are associated with spatial variations in stress, we expect the largest fibre body forces to be associated with the edges of stress 'hotspots' and thus moderate stress values.

To determine the spatial dependence of the fibre normal stress correlations, we have also considered single-point correlations of the fibre stresses and various flow quantities as a function of the distance from the wall. We define the single-point correlation as:

$$\rho = \frac{\overline{AB}}{A'B'}, \tag{5.5}$$

where A and B are the two quantities of interest, the overbar denotes the mean, and the prime denotes the r.m.s. of the quantity fluctuations. In figure 15, we present

the single-point correlation ρ of the fibre stress τ_{33} and the fluctuation velocities and velocity gradient components as well as the correlation of the fibre body force $\partial\tau_{ij}/\partial x_j$ with the fluctuation velocities. The single-point correlations of the fibre stress with the flow quantities show that τ_{33} is correlated with flows having low v' and w' throughout the near-wall region, as well as positive $\partial w/\partial z$, negative $\partial v/\partial y$ and small $\partial u/\partial x$. The correlations are somewhat different for the viscous sublayer with τ_{33} being related to positive $\partial w/\partial z$, negative $\partial u/\partial x$ and small $\partial v/\partial y$. We observe similar profiles for τ_{22}. These profiles show that the correlations observed in the scatter plots at $y^+ = 30$ are representative of the near-wall region in the flow.

With the exception of the the wall-normal velocity near the wall, the correlations of the fibre body force and fluctuation velocity components show that the fibre body forces are anti-correlated with velocity fluctuations. This result suggests that fibres act to oppose velocity fluctuations in all directions, except to weakly accelerate wall-normal fluctuations close to the wall ($y^+ < 5$). However, in this region the wall-normal velocity flucuations are nearly zero. These results differ slightly from what is seen in the polymer case: the weak accelerations in the wall-normal velocity for $y^+ < 5$ are observed, but body forces due to polymer stress are also strongly positively correlated with u' in the region $y^+ < 20$ and thus act to enhance fluctuations (Dubief *et al.* 2003) in a way that fibres do not.

To more clearly illustrate the details of the fibre–flow interactions suggested by the scatter plots and single-point correlations, we consider instantaneous visualizations of the flow field and the correlated fibre quantities. In figure 16, the contours of the fibre normal stress τ_{22} are plotted in the (y, z)-plane along with the projection of the velocity vectors into this plane. The region of largest stress corresponds to the stagnation region between vortices. In the adjacent figure, the contours of the fibre body force are plotted with the velocity vectors, showing an opposition to the local fluid motion. Lastly, we plot the eigenvector associated with the largest eigenvalue of the orientation tensor in combination with stress contours. This vector corresponds to the most probable direction of orientation. If equal to unity, the fibre is completely aligned in that direction. Figure 16(c) shows projections of this vector in the (y, z)-plane along with contours of the fibre stress τ_{22}. Large vectors correspond to fibres having complete alignment in the (y, z)-plane. As expected, the region of large τ_{22} corresponds to strong fibre alignment in the y-direction.

There are also correlations between the shear stresses τ_{13} and τ_{23} and decelerations due to the fibre body force. We have also found correlations of these stresses with extension (not shown) and in the case of τ_{13}, $\partial u/\partial z$. Visualizations of the flow field have shown that shear stress 'hotspots' are also associated with intervortex regions. Large values of τ_{23} result when fibres are confined strongly to the (y, z)-plane extensions, but have alignments that are not colinear with the y- or z-axis. Regions of large τ_{13} are associated with similar events in the (x, z)-plane that arise from the impact of downdrafts of fluid with the wall that give rise to large values of $\partial u/\partial z$.

Based on these observations, in figure 17 we present a diagram of the mechanism by which rigid fibres reduce turbulent drag. Instantaneous visualizations of the flow field show that high stress regions are confined to intervortex regions and are most pronounced in regions of intense vortex activity. These regions disappear when the vortex structures are weakened. Since the high stresses are due to strong planar alignment, we infer that the fibres are reoriented in the flow direction after the vortex structures are weakened. Visualizations of the principal axis of the fibre orientation tensor as a function of time (not shown) have demonstrated that this is the case. Some high-stress regions persist even after the vortices are weakened owing to the

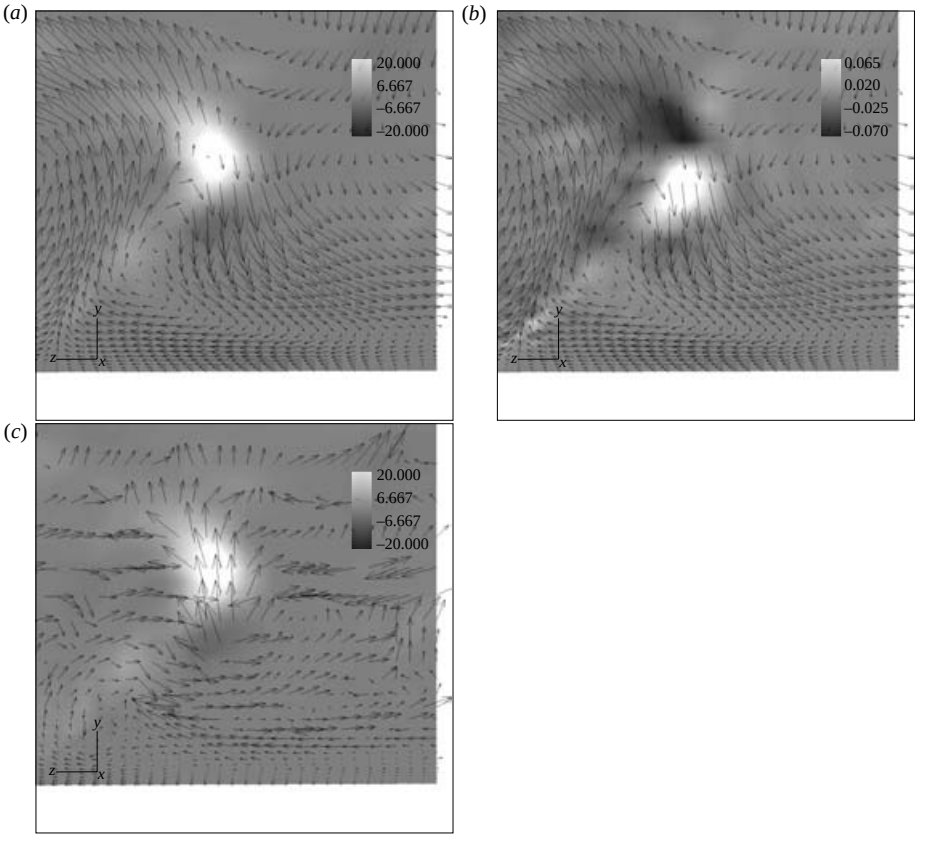

FIGURE 16. (*a*) Contours of fibre stress τ_{22} and (*b*) fibre y-body force with (y, z)-plane projection of velocity vectors. (*c*) Contours of fibre stress τ_{22} with (y, z)-plane projection of primary orientation axis vector.

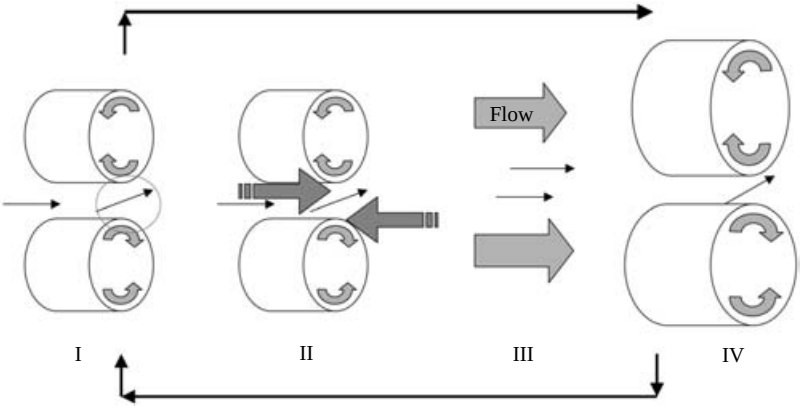

FIGURE 17. Schematic of mechanism for fibre-induced drag reduction. I. Fibres align in intervortex regions. *II*. Fibres generate large stresses and body forces that oppose vortex motion. *III*. Vortex stuctures are dissipated and fibres realign in flow direction. IV. Vortex structures re-emerge and cycle repeats.

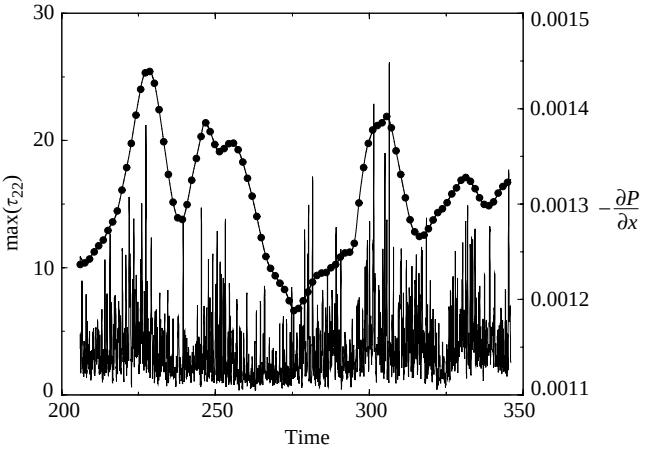

FIGURE 18. Time history of pressure drop through channel (circles) and maximum value of fibre stress τ_{22} (solid line).

lag in this reorientation process. After the fibres reorient in the flow direction, the reduction in local fibre stress allows the vortices to re-emerge and the turbulence is sustained in a weakened state.

To illustrate these dynamics, in figure 18 we present the time history of the pressure drop through the channel and the maximum value of the fibre stress τ_{22}. The pressure drop is directly related to the intensity of the near-wall vortices, with high pressure drops being indicative of stronger vortex structures. The maximum value of the fibre stress τ_{22} is a rough measure of alignment with large values being associated with orientation in the (y, z)-plane. There is a qualitative correspondence between the maxima and minima of the pressure drop and fibre stress histories, with 'bursts' of large fibre stress followed by reductions in pressure drop in accord with the mechanism described above.

In order to verify that the drag reduction is due to the proposed mechanism, we have performed a series of numerical experiments using the hybrid closure to isolate the contributions to drag reduction due to various stress components. In these experiments we have set certain contributions to the divergence of the extra stress related to particular stress components to zero. In figure 19, we present pressure drop versus time for various experiments. The simulations were performed using a fibre aspect ratio of 100, a Péclet number of 1000 and $nL^3 = 18$. Removing the contributions of τ_{22} to the fibre y-body force and τ_{33} to the fibre z-body force reduced the drag reduction from approximately 18% to 8%. By removing the contribution of τ_{22} to the fibre y-body force and all of the fibre z-body force (i.e. $\partial \tau_{3j}/\partial x_j = 0$), we obtained less than 1% drag reduction. This result suggests that the fibres reduce drag only via these four stress components and by the mechanisms outlined above, with roughly half of the drag reduction arising from the contributions of the two shear stresses. Since it is more likely that fibres will align in the (y, z)-plane as opposed to completely in the y- or z-directions, this result is not surprising.

6. Variation of rheological parameters

In this section, we consider the impact of variation of fibre parameters on the drag reduction performance. For this work, we have chosen to use a coarse mesh

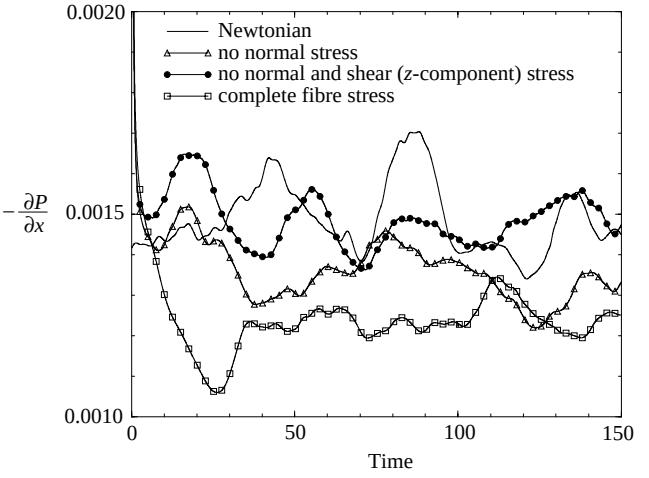

FIGURE 19. Pressure drop versus time for numerical experiments. Contributions to fibre body force removed as denoted in key.

resolution ($64 \times 129 \times 32$) as well as the computationally inexpensive hybrid closure in order to simulate a larger range of parameter space. We will consider the effects of suspension elasticity (rotary Péclet number), concentration, fibre aspect ratio, and the closure approximation in the following subsections. In each of these cases, we have used a Newtonian turbulent flow at a Reynolds number of 7500 as the initial flow for the fibre simulation of interest unless otherwise noted. We will always compare drag reductions for any given parameter set to a Newtonian flow at the effective Reynolds number defined using the suspension viscosity at the wall.

6.1. *Effect of rotary Péclet number or suspension elasticity*

A central motivation for this work was to determine the importance and effect of the suspension elasticity on drag reduction performance. We have focused on the moderate to high Péclet region for several reasons. Most importantly, the rheological model we employ is invalid for the low Péclet regime at the semi-dilute concentration that we have considered. Additionally, the effective viscosity is strongly increased at low Péclet numbers, making it difficult to maintain a sufficiently large effective Reynolds number to sustain turbulence. By focusing on the range of Péclet between 50 and ∞, we are able to remain within the range of validity of our rheological model and minimize effective Reynolds-number effects. The Newtonian turbulence statistics at Reynolds numbers of 6100 and 7500 (the upper and lower bounds of our effective Reynolds numbers) are not significantly different, nor do they introduce any resolution issues.

We performed a series of simulations as described in table 3 in which the value of Pe was varied while keeping all other parameters constant ($nL^3 = 18$ and an aspect ratio of 100). From these results, we observe that elasticity is not necessary for drag reduction as non-Brownian fibres are drag reducing. Non-Brownian fibres also give the most drag reduction suggesting that elasticity has a negative effect on drag-reduction performance. This result agrees with the results obtained by den Toonder *et al.* (1997) using a phenomenological model for elastic stresses.

Both the total wall shear stress (table 3) and the fibre contribution to the wall shear stress is increased as the Péclet number is decreased (figure 20). The mean velocity profiles also shown in figure 20 indicate that our effective viscosity scaling is correct

Péclet	μ_{eff}	Re_{eff}	Drag reduction (%)
50	1.23	6100	11.7
100	1.15	6497	13
1000	1.06	7100	18.5
∞	1.04	7200	19

TABLE 3. Effect of rotary Péclet number on drag reduction, $nL^3 = 18$ and $r_e = 100$. See text for results of matched effective Reynolds test using $Pe = 100$.

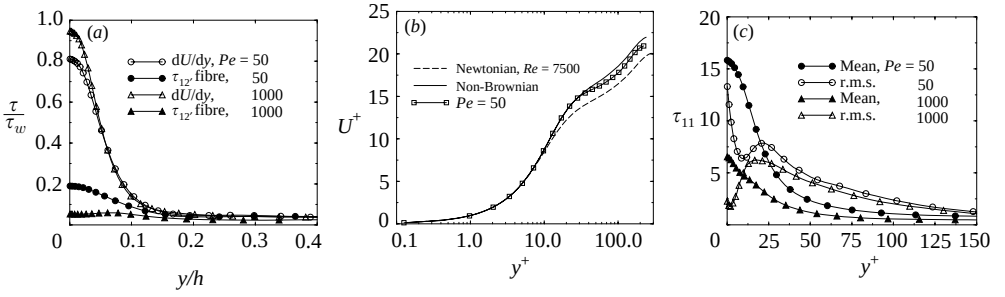

FIGURE 20. Effect of variation of suspension elasticity. (*a*) Viscous and fibre contributions to shear stress for $Pe = 50$ and $Pe = 1000$; (*b*) mean velocity profiles for $Pe = \infty$ and $Pe = 50$; (*c*) mean stress and r.m.s. stress fluctuations for $Pe = 50$ and $Pe = 1000$. All cases using hybrid closure, $r_e = 100$ and $nL^3 = 18$.

and that the effect of increasing the Péclet number is to increase the drag reduction and to shift the log-law region upwards. To clarify the effect of elasticity, we also consider the mean and r.m.s. fluctuations of the fibre normal stress τ_{11} in figure 20. We see that mean stresses and the fluctuations in the case of $Pe = 50$ are larger than those in the $Pe = 1000$ case since the elastic stresses are now significant. However, the fluctuations relative to the mean value are strongly decreased in the lower Péclet case in the range of $y^+ = 10$ to 50. We have observed similar trends for the fluctuations of the other normal stress components. These observations are in agreement with the results of Manhart (2003). These results suggest that the primary effect of increasing the suspension elasticity is to increase the near-wall fibre extra shear stress, leading to an increase in drag, but also to reduce the strength of extensional stress 'bursts' associated with drag reduction.

To confirm that the trend we have observed is not an artefact of the simultaneous shift in Péclet and effective Reynolds numbers, we have completed a simulation in which we attempted to match the effective Reynolds number at the wall for $Pe = 1000$ of 7100 for a $Pe = 100$ suspension. This test required an increase of the Newtonian base state Reynolds number to 8100. Using this value of Re, we obtained an effective viscosity at the wall of 1.15, giving an effective Reynolds number of 7070 and a drag reduction of 13.2%, which is less than that obtained using $Pe = 1000$ fibres at an approximately equal effective Reynolds number. This result suggests that the decrease in drag reduction with decreased Péclet is not an artefact of the suspension shear-thinning behaviour.

6.2. *Effect of concentration*

The effect of concentration is shown in table 4. For this series of simulations, $Pe = 1000$ and the aspect ratio was 100. The primary effect of increasing the volume

nL^3	μ_{eff}	Re_{eff}	Drag reduction (%)
5	1.01	7425	7.4
9	1.03	7301	13.2
18	1.06	7100	18.5
36	1.12	6707	26.2

TABLE 4. Effect of concentration on drag reduction. $Pe = 1000$ and $r_e = 100$.

r_e	ϕ	μ_{eff}	Re_{eff}	Drag reduction (%)
30	0.08	1.34	5597	10.8
50	0.03	1.15	6521	11.7
75	0.0135	1.08	6944	15.1
100	0.0075	1.06	7100	18.5

TABLE 5. Effect of fibre aspect ratio on drag reduction. $nL^3 = 18$ and $Pe = 1000$.

fraction is to increase the magnitude of the fibre extra stresses. We have shown in the previous section that drag-reduction performance is closely correlated to resistance to extensional motions, and for fibres the extensional viscosity is linearly proportional to nL^3. We do not see a linear increase in drag reduction behaviour, but this may be due to the details of the resulting flow behaviour and fibre dynamics. We have not increased the value of nL^3 beyond 36 since the assumption $nL^3 \ll r_e$, which is the definition of the semi-dilute regime, is questionable. For larger values of nL^3, the resulting isotropic concentrated suspension would need to be modelled in a way that would account for hindered fibre rotations. Both the resulting fibre dynamics and stresses would be substantially different to those presented here (Doi & Edwards 1986).

We have also considered the effect of fibre–fibre interactions by completing a simulation using the semidilute stress tensor (2.28 and 2.29) of Shaqfeh & Frederickson (1990) that accounts for fibre–fibre interactions in the non-Brownian limit. The effect of including hydrodynamic interactions in this manner for the non-Brownian case is to increase the magnitude of the stress by roughly 30%, but not to modify the fibre dynamics directly (other than through modified flow interactions). In this case, we obtain a drag reduction of 20.3% and an effective wall viscosity of 1.04, giving an effective Reynolds number of 7180. The use of the dilute stress scaling with semidilute values of nL^3 also gives statistical results (not shown) that are quantitatively similar to those using the more rigorous semi-dilute stress scaling. We can conclude that the effect of fibre–fibre interactions on the results presented here is minimal, at least in the non-Brownian limit.

6.3. *Effect of aspect ratio*

We consider the effect of aspect ratio in table 5. Reducing the aspect ratio modifies both the dynamic behaviour of the fibres and the fibre extra stress. We see that the primary effect of decreasing the aspect ratio is an increase in the effective viscosity and a reduction in the drag reduction effectiveness. This effect can be explained by examining the behaviour of the fibres in the mean flow near the walls, which is a

Closure	μ_{eff}	Re_{eff}	Drag reduction (%)
Hybrid	1.06	7100	15.8
IBOF	1.12	6710	13.4

TABLE 6. Effect of closure approximation on drag reduction. $Pe = 1000$, $nL^3 = 18$, $r_e = 100$.

shear flow; as a result, the Jeffrey solution for the fibre dynamics is applicable. As discussed in Petrich, Koch & Cohen (2000), the fibre extra shear stress scales as $nL^3 r_e^{-1}$. As the aspect ratio is decreased, the total extra shear stress at the wall is increased, reducing the drag-reduction effectiveness. Additionally, as the aspect ratio is decreased, extensional stresses are decreased (Brenner 1974) and this effect may also be responsible for the lower levels of drag reduction observed.

The experimental study of Radin *et al.* (1975) observed that for a given concentration, particles with an aspect ratio of less than 25 to 35 did not give drag reduction and that increasing the aspect ratio improved drag reduction effectiveness. In their experiments, the drag reductions were determined using pressure drop measurements for flows at a constant Newtonian Reynolds number in a manner analogous to the numerical experiment performed here. Our test shows that the drag reduction is reduced when aspect ratio is decreased, though we still see a modest level of drag reduction at $r_e = 30$.

6.4. *Effect of closure approximation*

In order to make the numerical solution of the fibre dynamics tractable, we employed a closure approximation for the fourth moment of the orientation vector, a_{ijkl}. For this test, we have considered $Pe = 1000$ fibres with a concentration $nL^3 = 18$ and aspect ratio of 100, using the $80 \times 141 \times 80$ mesh. The effective viscosities and drag reductions are given in table 6.

As might be expected from the small difference in drag reductions, we see only modest effects on the flow statistics and mechanistic correlations, as shown in figure 21. The mean velocity profile and r.m.s. velocity fluctuations are qualitatively similar. The single-point correlations for fibre stresses and flow quantities as well as the fibre work correlations are also remarkably similar. Based on these results, we conclude that the choice of closure approximation has no effect on the mechanism presented in the previous section and only a modest effect on the drag-reduction behaviour.

However, there is a significant difference in the mean stress profiles, shown in figure 22. The more accurate IBOF closure gives qualitatively different profiles for both the mean stresses, especially for the first normal stress difference in the region $y^+ < 20$. To explain the origin of this effect, we have considered the stresses generated in simple shear using the mean shear rate obtained in the turbulent channel-flow simulations. We see that the resulting first normal stress and shear stress profiles are nearly identical to the mean values at the wall in the turbulent channel flow. The differences in the simple shear flow behaviour are due to the weakened flow alignment predicted by the more accurate IBOF closure as compared to the hybrid closure; since the fibres are on average less strongly oriented in the 1-direction the first normal stress difference is decreased and the shear stress is increased. Since the mean stress profiles begin to attain the same shape by $y^+ = 20$, this result suggests that the difference in the mean stress profiles is primarily due to the difference in the shear-dominated near-wall stress behaviour. The result also suggests that the near-wall stresses do not

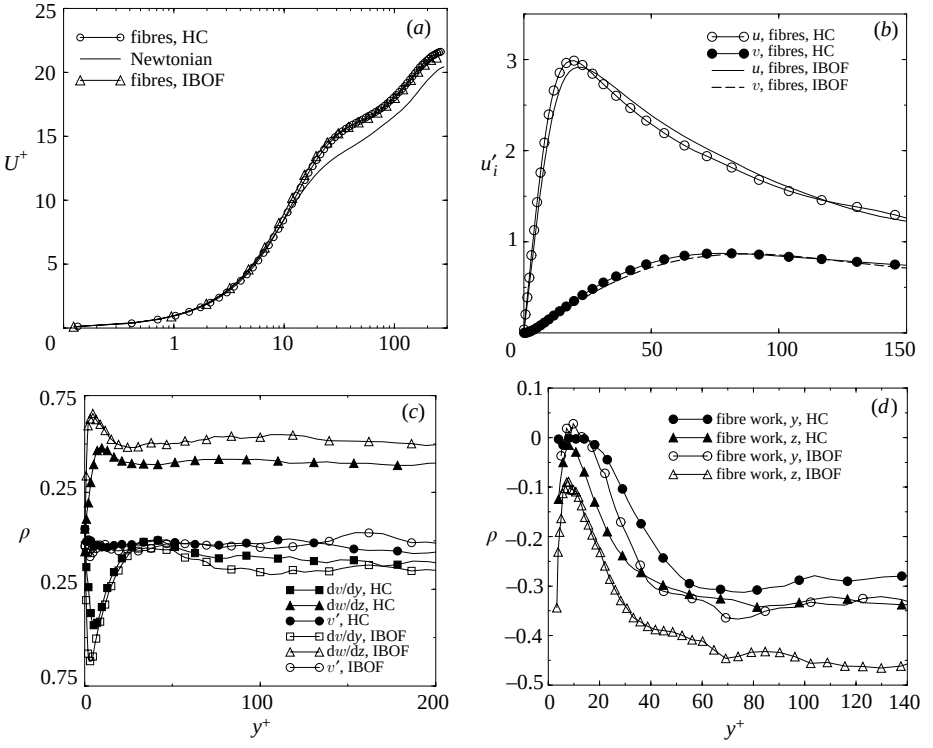

FIGURE 21. Effect of closure approximation on flow statistics. (*a*) Mean velocity and (*b*) r.m.s. velocity fluctuations; (*c*) single-point correlations of fibre stress and velocity and (*d*) scalar product of velocity and divergence of fibre stress or 'fibre work'.

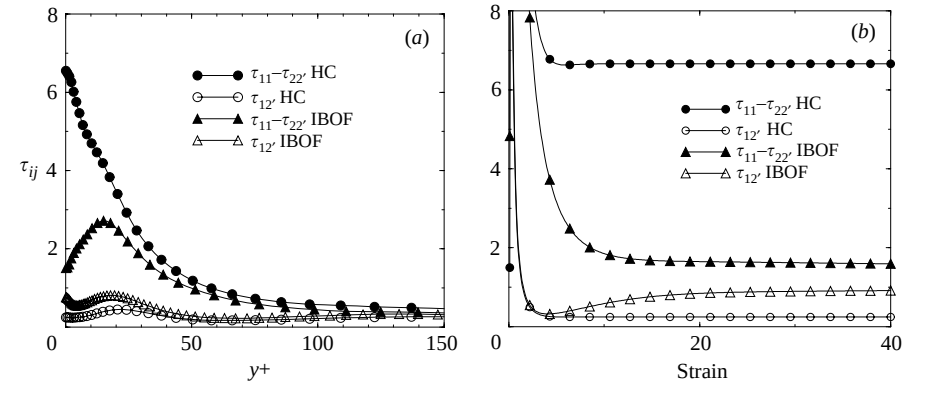

FIGURE 22. Effect of closure approximation on fibre stress statistics. (*a*) Fibre mean stresses. (*b*) Time evolution of fibre stresses in simple shear flow at mean shear rate obtained from turbulent channel simulations. Note correspondence of steady shear stress values and mean values of stress at wall in turbulence simulation.

have a significant effect on the drag reduction, and that modified dynamics of the more accurate closure have only a modest impact on the fibre stresses in the buffer layer since the mean stresses and the r.m.s. stress fluctuations (not shown) in that region are qualitatively similar but slightly lower. Based on these observations, we

conclude the drag reduction statistics and mechanisms we have presented here have only a weak dependence on the choice of closure approximation.

7. Summary and discussion

We have presented a detailed investigation of drag reduction using rigid fibre additives, modelled using the appropriate constitutive equation with two different closure approximations. The central findings of the work are that elasticity has a negative impact on drag-reduction effectiveness and that fibres create drag reduction via an extensional mechanism in inter-vortex regions. Fibres strongly align in the (y, z)-plane, generating large normal and shear stresses. These stresses create a force opposite to Newtonian accelerations in the spanwise and wall-normal directions that weakens the near-wall vortex structures giving drag reduction. Subsequent realignment of the fibres in the flow direction allows the vortices to reform in the absence of fibre stresses, allowing weakened turbulence to be sustained. As the amount of drag reduction is increased, the near-wall vortices become weaker and move farther apart, ultimately limiting the drag reduction effectiveness of rigid fibres since the mechanism presented here requires the interaction of multiple vortices.

The experimental behaviour of drag-reducing fibre suspensions as discussed by Radin *et al.* (1975) may be explained in part by our results. Specifically, these authors found that, unlike the polymeric case, there is no onset phenomenon associated with fibrous drag reduction. As explained by Sureshkumar *et al.* (1997), the existence of a critical Weissenberg number for polymeric flows appears to be associated with coil–stretch transition. In the case of fibres, stresses are immediately added as soon as the fibres achieve alignment in extensional regions. This effect may very well give rise to a prolonged transition regime, as discussed by Radin *et al.* (1975), instead of the abrupt onset as seen with polymers.

We have made few comparisons to experimental data since there is little data available for rigid rodlike additives at the relatively low Reynolds numbers and concentrations we have considered; there is certainly none available with modern flow instrumentation such as particle image velocimetry. The best comparison we can make is with the data of Sasaki (1991), in which schizophyllan polysaccharide gave a drag reduction of 6.5% at a Newtonian Reynolds number of 6800 in a 6 mm inner diameter pipe. For the molecular weight and concentration reported for this experiment, we estimate that $nL^3 \approx 1.5$ and the aspect ratio is 245. The Péclet number based on the wall shear rate in this experiment was approximately 50. We found in our study of concentration that fibres with $Pe = 1000$, $r_e = 100$ and $nL^3 = 5$ gave 7.4% drag reduction. Based on the trends presented in our rheological parameter study, we expect that the calculated drag reduction would be slightly lower than the experimental value.

Lastly, we motivated our work with the synergy effect observed using mixtures of fibres and polymers to achieve drag reductions exceeding the sum of those obtained using either additive alone. Since this effect has been observed using mixtures of rigid polymers and flexible polymers, we believe that the model presented here will allow us to investigate this phenomenon. We will consider drag reductions using mixtures in an forthcoming work.

We thank Christopher White and Vincent Terrapon for helpful discussions. This work is sponsored by the Defense Advanced Research Projects Agency, Advanced

Technology Office, Friction Drag Reduction Program, DARPA order no. K042/31, K042/13, N115/00. Issued by DARPA/CMO, contract no. MDA972-01-C-0041.

REFERENCES

Advani, S. & Tucker, C. 1987 The use of tensors to describe and predict fibre orientation in short fibre composites. *J. Rheol.* **31**, 751–784.

Advani, S. & Tucker, C. 1990 Closure approximations for three-dimensional structure tensors. *J. Rheol.* **34**, 367–386.

Ahmed, A. & Elgobashi, S. 2000 On the mechanisms of modifying the structure of turbulent homogeneous shear flows by dispersed particles. *Phys. Fluids* **12**, 2906–2930.

Azaiez, J. 2000 Linear stability analysis of free shear flows of fibre suspensions. *J. Fluid Mech.* **404**, 179–209.

Batchelor, G. 1959 Small-scale variation of convected quantities like temperature in a turbulent fluid. *J. Fluid Mech.* **5**, 113–133.

Beris, A. & Dimitropoulos, C. 1999 Pseudospectral simulation of turbulent viscoelastic channel flow. *Comput. Methods Appl. Mech. Engng* **180**, 365–392.

Blackburn, H., Mansour, N. & Cantwell, B. 1996 Topology of fine scale motions in turbulent channel flow. *J. Fluid Mech.* **310**, 269–292.

Brenner, H. 1974 Rheology of a dilute suspension of axisymmetric Brownian particles. *Intl J. Multiphase Flow* **1**, 195–341.

Choi, H., Moin, P. & Kim, J. 1994 Active turbulence control for drag reduction in wall-bounded flows. *J. Fluid Mech.* **262**, 75–110.

Chung, D. & Kwon, T. 2001 Improved model of orthotropic closure approximation for flow-induced fibre orientation. *Polymer Comput.* **22**, 636–649.

Chung, D. & Kwon, T. 2002 Invariant-based optimal fitting closure approximation for the numerical prediction of flow-induced fibre orientation. *J. Rheol.* **46**, 169–194.

Cintra, J. & Tucker, C. 1995 Orthotropic closure approximations for flow-induced fibre orientation. *J. Rheol.* **39**, 1095–1122.

Dimitropoulos, C., Sureshkumar, R. & Beris, A. 1998 Direct numerical simulation of viscoelastic turbulent channel flow exhibiting drag reduction: effect of variation of rheological parameters. *J. Non-Newtonian Fluid Mech.* **79**, 433–468.

Dimitropoulos, C., Sureshkumar, R., Beris, A. & Handler, R. 2001 Budgets of Reynolds stress, kinetic energy and streamwise enstrophy in viscoelastic turbulent channel flow. *Phys. Fluids* **13**, 1016–1027.

Dingilian, G. & Ruckenstein, E. 1974 Positive and negative deviations from additivity in drag reduction of binary dilute polymer solutions. *AIChE J.* **20**, 1222–1224.

Doi, M. & Edwards, S. 1986 *The Theory of Polymer Dynamics*. Oxford University Press.

Dubief, Y. 2002 Numerical simulation of turbulent polymer solutions. In *Center for Turbulence Research Annual Briefs*, pp. 1–12. NASA Ames/Stanford University.

Dubief, Y. & Delcayre, F. 2000 On coherent-vortex identification in turbulence. *J. Turbulence* **1**, 011.

Dubief, Y. & Lele, S. 2001 Direct numerical solution of polymer flow. In *Center for Turbulence Research Annual Briefs*, pp. 197–298. NASA Ames/Stanford University.

Dubief, Y., Terrapon, V., White, C., Shaqfeh, E., Moin, P. & Lele, S. 2004*a* New answers on the interacton between polymers and vortices in turbulent flows. *Flow Turbulence Combust.* (in press).

Dubief, Y., White, C., Terrapon, V. E., Shaqfeh, E., Moin, P. & Lele, S. 2004*b* On the coherent drag-reducing and turbulence-enhancing behaviour of polymers in wall flows. *J. Fluid Mech.* **514**, 271–280.

Fan, F. & Ahmadi, G. 2000 Wall deposition of small ellipsoids from turbulent air flows – a Brownian dynamics simulation. *J. Aerosol Sci.* **31**, 1205–1229.

Feng, J. & Joseph, D. 1995 The unsteady motion of solid bodies in creeping flows. *J. Fluid Mech.* **303**, 83–102.

Folgar, F. & Tucker, C. 1984 Orientation behavior of fibres in concentrated suspensions. *J. Reinforced Plastics Composites* **3**, 98–119.

Hinch, E. & Leal, L. 1972 The effect of Brownian motion on the rheological properties of a suspension of non-spherical particles. *J. Fluid Mech.* **52**, 683–712.

Hinch, E. & Leal, L. 1975 Constitutive equations in suspension mechanics. Part 1. General formulation. *J. Fluid Mech.* **71**, 481–495.

Hinch, E. & Leal, L. 1976 Constitutive equations in suspension mechanics. Part 2. Approximate forms for a suspension of rigid particles affected by Brownian rotations. *J. Fluid Mech.* **76**, 187–208.

Jimenez, J. & Moin, P. 1991 The minimal flow unit in near-wall turbulence. *J. Fluid Mech.* **225**, 213–240.

Jimenez, J. & Pinelli, A. 1999 The autonomous cycle of near-wall turbulence. *J. Fluid Mech.* **389**, 335–359.

Joseph, D. 1990 *Fluid Dynamics of Viscoelastic Liquids*. Springer.

Kale, D. & Metzner, A. 1976 Turbulent drag reduction in dilute fibre suspensions: mechanistic considerations. *AIChE J.* **22**, 669–674.

Kim, J., Moin, P. & Moser, R. 1987 Turbulent statistics in a fully developed turbulent channel flow. *J. Fluid Mech.* **177**, 133–166.

Kim, S. & Karrila, S. 1991 *Microhydrodynamics: Principles and Selected Applications*. Butterworth–Heinemann.

Koch, D. 1995 A model for orientational diffusion in fibre suspensions. *Phys. Fluids* **7**, 2086–2088.

Koch, D. & Hill, R. 2001 Inertial effects in suspension and porous media flows. *Annu. Rew. Fluid Mech.* **33**, 619–647.

Koch, D. & Shaqfeh, E. 1990 The average rotation rate of a fibre in the linear flow of a semidilute suspension. *Phys. Fluids* A **2**, 2093–2102.

Kravchenko, A., Choi, H. & Moin, P. 1993 On the relation of near-wall streamwise vortices to wall skin friction in turbulent boundary layers. *Phys. Fluids* A **5**, 3307–3309.

Kulick, J., Fessler, J. & Eaton, J. 1994 Particle response and modification in fully turbulent channel flow. *J. Fluid Mech.* **277**, 109–134.

Larson, R. 1999 *The Structure and Rheology of Complex Liquids*. Oxford University Press.

Le, H. & Moin, P. 1991 An improvement in fractional step methods for the incompressible Navier–Stokes equations. *J. Comput. Phys.* **92**, 369–379.

Lee, C. & Kim, J. 2002 Control of the viscous sublayer for drag reduction. *Phys. Fluids* **14**, 2523–2529.

Lee, W., Vaseleski, R. & Metzner, A. 1974 Turbulent drag reduction in polymeric solutions containing suspended fibres. *AIChE J.* **20**, 128–133.

Li, Y., McLaughlin, J., Kontomaris, K. & Portela, L. 2001 Numerical simulation of particle laden turbulent channel flow. *Phys. Fluids* **13**, 2957–2967.

Lumley, J. 1969 Drag reduction by additives. *Annu. Rev. Fluid Mech.* **1**, 367–384.

McComb, W. & Chan, K. 1985 Laser-Doppler anemometer measurements of turbulent structure in drag-reducing fibre suspensions. *J. Fluid Mech.* **152**, 455–478.

Malhotra, J., Deshmukh, S. & Singh, R. 1987 Turbulent drag reduction by polymer–fibre mixtures. *J. Appl. Polymer Sci.* **33**, 2467–2478.

Manhart, M. 2003 Rheology of suspensions of rigid-rod like particles in turbulent channel flow. *J. Non-Newtonian Fluid Mech.* **112**, 269–293.

Metzner, A. 1977 Polymer solution and fibre suspension rheology and their relationship to turbulent drag reduction. *Phys. Fluids* **10**, S145–S149.

Min, T., Yoo, J. & Choi, H. 2001 Effect of spatial discretization schemes on numerical studies of viscoelastic flows. *J. Non-Newtonian Fluid Mech.* **100**, 27–47.

Nayak, R. 1998 Molecular simulation of liquid crystal polymer flow: a wavelet-finite element analysis. PhD thesis, MIT.

Petrich, M., Koch, D. & Cohen, C. 2000 An experimental determination of the stress–microstructure relationship in semi-concentrated fibre suspensions. *J. Non-Newtonian Fluid Mech.* **95**, 101–133.

Pirih, R. & Swanson, W. 1972 Drag reduction and turbulence modification in rigid particle suspensions. *Can. J. Chem. Engng* **50** 221–227.

Qi, D. & Luo, L. 2002 Transitions in rotations of a nonspherical particle in a three-dimensional moderate Reynolds number Couette flow. *Phys. Fluids* **14**, 4440–4443.

Radin, I., Zakin, J. & Patterson, G. 1975 Drag reduction in solid–fluid systems. *AIChE J.* **21**, 358–371.

Rahnama, M., Koch, D. & Shaqfeh, E. 1995 The effect of hydrodynamic interactions on the orientation distribution in a fibre suspension subject to a simple shear flow. *Phys. Fluids* **7**, 487–506.

Reddy, G. & Singh, R. 1985 Drag reduction effectiveness and shear stability of polymer–polymer and polymer–fibre mixtures in recirculatory turbulent flow of water. *Rheol. Acta.* **24**, 296–311.

Robertson, A. & Mason, S. 1957 The flow characteristics of dilute fibre suspensions. *TAPPI J.* **40**, 326–334.

Sasaki, S. 1991 Drag reduction effect of rod-like polymer solutions. i. Influences of polymer concentration and rigidity of skeletal back bone. *J. Phys. Soc. Japan* **60**, 868–878.

Schiek, R. & Shaqfeh, E. 1995 A nonlocal theory for stress in bound, Brownian suspensions of slender rigid fibres. *J. Fluid Mech.* **296**, 271–324.

Seyer, F. & Metzner, A. 1969 Turbulence phenomena in drag reducing systems. *AIChE J.* **15**, 426–434.

Shaqfeh, E. & Frederickson, G. 1990 The hydrodynamic stress in a suspension of rods. *Phys. Fluids* A **2**, 7–24.

Shaqfeh, E. & Koch, D. 1990 Orientational dispersion of fibres in extensional flows. *Phys. Fluids* A **2**, 1077–1093.

Sreenivasan, K. & White, C. 2000 The onset of drag reduction by dilute polymer additives and the maximum drag reduction asymptote. *J. Fluid Mech.* **409**, 149–164.

Suen, J., Joo, Y. & Armstrong, R. 2002 Molecular orientation effects in viscoelasticity. *Annu. Rew. Fluid Mech.* **34**, 417–444.

Sureshkumar, R., Beris, A. & Handler, R. 1997 Direct numerical simulations of turbulent channel flow of a polymer solution. *Phys. Fluids* **9**, 743–755.

Szeri, A. & Leal, L. 1994 A new computational method for the solution of flow problems in microstructured fluids. Part 2. Inhomogeneous shear flow of a suspension. *J. Fluid Mech.* **262**, 171–204.

Tabor, M. & deGennes, P. 1986 A cascade theory of drag reduction. *Europhys. Lett.* **2**, 519–522.

Terrapon, V., Dubief, Y., Moin, P., Shaqfeh, E. & Lele, S. 2004 Simulated polymer stretch in a turbulent flow using Brownian dynamics. *J. Fluid Mech.* **504**, 61–71.

den Toonder, J., Hulsen, M., Kuiken, G. & Nieuwstadt, F. 1997 Drag reduction by polymer additives in a turbulent pipe flow: numerical and laboratory experiments. *J. Fluid Mech.* **337**, 193–231.

Virk, P., Mickley, H. & Smith, K. 1970 The ultimate asymptote and mean flow structures in tom's phenomenon. *Trans. ASME* E: *J. Appl. Mech.* **37**, 488–493.

Zhang, H., Ahmadi, G., Fan, F. & McLaughlin, J. 2001 Ellipsoidal particles transport and deposition in turbulent channel flows. *Intl J. Multiphase Flow* **27**, 971–1009.